Alternative splicing of auxiliary β2-subunits stabilizes Cav2.3 Ca^{2+} channel activity in continuously active midbrain dopamine neurons

Anita Siller[1], Nadja T. Hofer[1], Giulia Tomagra[3], Nicole Wiederspohn[4], Simon Hess[5], Julia Benkert[4], Aisylu Gaifullina[4], Desiree Spaich[4], Johanna Duda[4], Christina Pötschke[4], Kristina Vilusic[1], Eva Maria Fritz[1], Toni Schneider[2], Peter Kloppenburg[5], Birgit Liss[4], Valentina Carabelli[3], Emilio Carbone[3], Nadine J. Ortner[1*] and Jörg Striessnig[1*]

[1]Department of Pharmacology and Toxicology, Institute of Pharmacy, Center for Molecular Biosciences Innsbruck, University of Innsbruck, Innsbruck, Austria;

[2]Institute of Neurophysiology, University of Cologne, Cologne, Germany;

[3]Department of Drug Science, NIS Centre, University of Torino, Torino, Italy;

[4]Institute of Applied Physiology, University of Ulm, Ulm, Germany;

[5]Institute for Zoology, Biocenter, CECAD, University of Cologne, Cologne, Germany.

***Correspondence:**
Nadine J. Ortner (nadine.ortner@uibk.ac.at; +43-512-507-58815) or Jörg Striessnig (joerg.striessnig@uibk.ac.at; +43-512-507-58800)

Keywords: Cav2.3, R-type Ca^{2+} channel, β-subunits, alternative splicing, dopaminergic neurons, Parkinson's disease

Number of words: 5376
Number of figures: 9 (plus 5 supplementary figures)

Abstract

In dopaminergic (DA) substantia nigra (SN) neurons Cav2.3 R-type Ca^{2+}-currents contribute to somatodendritic Ca^{2+}-oscillations. These may contribute to the selective degeneration of these neurons in Parkinson's disease (PD) since Cav2.3-knockout is neuroprotective in a PD mouse model. However, the typical Cav2.3 gating would predict complete channel inactivation during SN DA neuronal firing. Here we show that in tsA-201-cells the membrane-anchored β2-splice variants β2a and β2e stabilize Cav2.3 gating properties allowing sustained Cav2.3 availability during simulated pacemaking and enhanced Ca^{2+}-currents during bursts. We confirmed the expression of β2a and β2e-subunits in the SN and identified SN DA neurons. Patch-clamp recordings of SN DA neurons in mouse brain slices revealed R-type Ca^{2+}-currents similar to β2a- or β2e-stabilized Cav2.3-currents and recordings in cultured murine DA neurons confirmed their activity during pacemaking. Taken together, our data support an important (patho)physiological role of β-subunit alternative splicing for Cav2.3 Ca^{2+}-signaling in highly vulnerable SN DA neurons.

Introduction

Parkinson's disease (PD) is one of the most common neurodegenerative disorders. Its motor symptoms are characterized by progressive degeneration of dopamine (DA)-releasing neurons in the substantia nigra (SN), while neighboring DA neurons in the ventral tegmental area (VTA) remain largely unaffected (Damier et al., 1999; Giguère et al., 2018; Surmeier et al., 2017). Current PD therapy is only symptomatic and primarily based on the substitution of striatal DA by administration of L-DOPA or dopamine D2 receptor agonists. Unfortunately, none of the existing therapeutic approaches for PD patients is disease-modifying and can prevent disease progression (for review see Liss & Striessnig, 2019; Surmeier et al., 2011; Surmeier et al., 2017).

The development of novel neuroprotective strategies for the treatment of early PD requires the understanding of the cellular mechanisms responsible for the high vulnerability of SN DA neurons. Among these mechanisms elevated metabolic stress appears to play a central role (for review see Liss & Striessnig, 2019), eventually triggering lysosomal, proteasomal and mitochondrial dysfunction (Burbulla et al., 2017; Surmeier et al., 2017). Intrinsic physiological properties of SN DA neurons, in particular increased cytosolic DA levels and high energy demand due to large axonal arborisation favour metabolic stress (Bolam & Pissadaki, 2012; Liss & Striessnig, 2019). In addition, these neurons must handle a constant intracellular Ca^{2+}-load resulting from dendritic and somatic Ca^{2+}-oscillations triggered during their continuous electrical activity (Ortner et al., 2017; Surmeier et al., 2011). Dendritic Ca^{2+}-transients largely depend on the activity of voltage-gated Ca^{2+} channels, in particular Cav1.3 L-type (LTCCs) and T-type channels (Guzman et al., 2018). Cav1.3 channels can activate at subthreshold membrane potentials (Koschak et al., 2001; Lieb et al., 2014; Xu & Lipscombe, 2001) and do not completely inactivate during continuous pacemaking activity (Guzman et al., 2018; Guzman et al., 2009; Ortner et al., 2017). Some, but not all, in vivo studies (Liss & Striessnig, 2019) showed neuroprotection by the systemic administration of dihydropyridine (DHP) L-type channel blockers in 6-OHDA and MPTP animal models of PD thus further supporting a role of LTCCs as potential neuroprotective drug target. Based on these preclinical data and supporting observational clinical evidence (Liss & Striessnig, 2019), the neuroprotective potential of the DHP isradipine (ISR) was tested in a double-blind, placebo-controlled, parallel-group phase 3 clinical trial ("STEADY-PD III", NCT02168842; Biglan et al., 2017). This trial reported no evidence for neuroprotection by ISR. Several explanations have been offered for this negative outcome (Parkinson Study Group, 2020). One likely explanation is that voltage-gated Ca^{2+}-channels (Cavs) other than LTCCs also contribute to Ca^{2+}-transients in SN DA neurons. This is supported by the observation that only about 50% of the Ca^{2+}-transients are blocked by isradipine in the dendrites of SN DA neurons (Guzman et al., 2018) and that action potential-associated Ca^{2+}-transients in the soma appear to be even resistant to isradipine

82 (Ortner et al., 2017). Therefore, in addition to L-type, other types of Cavs expressed in SN DA
83 neurons (Branch et al., 2014; Evans et al., 2017; Philippart et al., 2016) may also contribute to
84 Ca^{2+}-induced metabolic stress in SN DA neurons. Cav2.3 (R-type) Ca^{2+}-channels are very
85 promising candidates. We have recently shown that SN DA neurons in mice lacking Cav2.3
86 channels were fully protected from neurodegeneration in the chronic MPTP-model of PD.
87 Moreover, we found that Cav2.3 is the most abundant Cav expressed in SN DA neurons, and
88 substantially contributes to activity-related somatic Ca^{2+}-oscillations (Benkert et al., 2019).
89 These findings make Cav2.3 R-type Ca^{2+} channels a promising target for neuroprotection in
90 PD.

91 SN DA neurons are spontaneously active, pacemaking neurons, either firing in a low-frequency
92 single-spike mode or transiently in a high-frequency burst mode (Grace & Bunney, 1984a,
93 1984b; Paladini & Roeper, 2014). During regular pacemaking their membrane potential is, on
94 average, rather depolarized ranging from about -70 mV after an action potential (AP) to about
95 -40 mV at firing threshold (Gantz et al., 2018; Guzman et al., 2018; Ortner et al., 2017). The
96 contribution of a particular Cav channel to Ca^{2+}-entry is therefore largely determined by its
97 steady-state inactivation properties, which determines its availability at these depolarized
98 voltages. In Cav2.3 channels expressed with auxiliary α2δ and various β-subunits steady-state
99 inactivation occurs at much more negative potentials being almost complete at voltages
100 positive to -50 mV. Moreover, Cav2.3 channels inactivate quickly during depolarizations (Jones
101 et al., 1998; Pereverzev et al., 2002; Soong et al., 1993; Williams et al., 1994; Yasuda et al.,
102 2004). Together these properties predict that most of the Cav2.3 channel current is inactivated
103 during continuous SN DA neuron pacemaking.

104 Here we directly addressed this question by stimulating Cav2.3 channel complexes using
105 command voltages simulating either SN DA neuron-like tonic pacemaking or brief burst
106 activity. As previously described for LTCCs (Ortner et al., 2017) we expressed Cav2.3
107 channels together with auxiliary subunits in tsA-201 cells because individual Ca^{2+}-current
108 components are difficult to resolve in patch-clamp recordings of SN DA neurons in slices. We
109 found that Cav2.3 currents rapidly decay when co-expressed with β3 and β4 subunits.
110 However, Cav2.3 remained active during continuous pacemaking in the presence of the β2a
111 and β2e splice variants, which stabilize steady-state inactivation of Cav2.3 at more positive
112 potentials (up to 35 mV more positive compared to β3) and considerably slow current
113 inactivation. In contrast, steady-state inactivation of Cav1.3 channels was largely unaffected
114 by β2a, suggesting that Cav1.3 availability is much less dependent on the presence of β2a
115 subunits. Using RNAScope we confirmed the presence of both, β2a and β2e transcripts in
116 identified mouse SN and VTA DA neurons and quantitative PCR analysis showed that β2-
117 subunits represent about 25% of all β-subunit transcripts in the SN and VTA with about 50%
118 comprising β2a and β2e variants. In patch-clamp recordings of SN DA neurons in mouse brain

119 slices we detected R-type Ca^{2+}-currents similar to β2a- or β2e-stabilized Cav2.3-currents and
120 recordings in cultured DA neurons confirmed R-type current activity during the pacemaking
121 cycle. Taken together, our data further support a role of Cav2.3 in SN DA neuron Ca^{2+}-signaling
122 and reveal an important (patho)physiological role of β-subunit alternative splicing.

123 **Results**

124 **SNX-482 inhibits Ca^{2+} current (I_{Ca}) and reduces spontaneous AP firing in cultured mouse**
125 **midbrain DA neurons**

126 We have recently shown that in mouse SN DA neurons Cav2.3 channels contribute to action
127 potential (AP)-induced somatic Ca^{2+}-oscillations. In Cav2.3-deficient mice the amplitude of the
128 Ca^{2+}-oscillations was decreased by about 50%. This continuous Ca^{2+} load can potentially
129 contribute to the high vulnerability of these neurons in PD (Benkert et al., 2019).

130 To further confirm the presence of functional Cav2.3 channels we investigated effects of the
131 Cav2.3 blocker SNX-482 on firing frequency and AP shape in spontaneously firing cultured
132 mouse DA midbrain neurons. We employed SNX-482 at a low concentration (100 nM) to inhibit
133 Cav2.3 current components (IC_{50}=30 nM) but spare L-type channels (IC_{50}>1 µM, Bourinet et
134 al., 2001; Newcomb et al., 1998). SNX-482 had profound effects on firing properties. In current-
135 clamp recordings it significantly reduced the spontaneous firing frequency from 4.1 ± 0.8 Hz
136 (control, n=10, N=3; 95% CI: 2.1-6.1) to 1.1 ± 0.2 Hz (SNX-482, n=10, 95% CI: 0.2-2.1,
137 p=0.0036, paired Student's t-test; Fig. 1A, B) and decreased the regularity of pacemaking
138 (coefficient of variation of the mean interspike interval increased from 0.25 ± 0.06 (control, 95%
139 CI: 0.15-0.39) to 0.78 ± 0.13 (SNX-482, 95% CI: 0.49-1.09, p=0.0032, paired Student's t-test;
140 Fig. 1B)). Slowing of firing was associated with hyperpolarization of the most negative voltage
141 reached during the afterhyperpolarization (AHP) immediately after the spike (AHP peak), which
142 decreased from -43.2 ± 1.3 mV (control, 95% CI: -45.8 - -40.7) to -47.0 ± 1.2 mV (SNX-482,
143 95% CI: -49.4 - -44.6, p=0.0005, paired Student's t-test; Fig. 1B). Other changes in the AP
144 waveform, which could represent indirect effects from the slowing of AP frequency or result
145 from inhibition of Cav2.3 channels, were also noted: a reduced mean AP half-width (control:
146 5.1 ± 0.3 ms, 95% CI: 4.4-5.8; SNX-482: 4.2 ± 0.3 ms, 95% CI: 3.7-4.8; p=0.0050, paired
147 Student's t-test), and a trend towards increased maximum time-derivative of voltage (control:
148 45.3 ± 4.9 mV/ms, 95% CI: 34.4-56.3; SNX-482: 74.3 ± 13.5 mV/ms, 95% CI: 47.0-101.5,
149 p=0.0625, paired Student's t-test, estimated from the phase-plane plot of Fig. 1C). The latter
150 is likely due to the recruitment of more voltage-gated Na^{+}-channels during the AP onset from
151 the more hyperpolarized interspike membrane potential (Guarina et al., 2018; Tomagra et al.,
152 2019).

153 We also isolated SNX-482-sensitive Cav2.3 currents in cultured DA midbrain neurons using
154 voltage-clamp experiments. In order to exclude that part of the Ca^{2+}-current inhibition by SNX-
155 482 could be attributed to the inhibition of L-type channels, we added SNX-482 (100 nM) after
156 the complete block of L-type currents (comprising about 25% of total Ca^{2+}-current, not shown)
157 by 3 µM isradipine (ISR). Ca^{2+}-currents were elicited by consecutive depolarizing 50-ms square
158 pulses to 0 mV from a holding potential of -70 mV every 10 s. Once stable recordings were

159 obtained in the presence of isradipine (see representative experiments in Fig. 2A, B), 100 nM
160 of SNX-482 were applied. Application of 100 nM SNX-482 significantly reduced non-L-type
161 currents by 41 ± 4 % (95% CI: 33-49, n=20, N=4, paired Student's t-test; p<0.001) (Fig. 2C)
162 corresponding to an absolute decrease of current amplitude from 529 ± 57 pA (95% CI: 409-
163 649) to 313 ± 33 pA (95% CI: 245-381, n=20, paired Students t-test p<0.01) (Fig. 2D). All
164 residual I_{Ca} components were blocked by adding 2 µM Cd^{2+} to the bath solution (Fig. 2A, B).

165 Primary cultures of DA neurons are not very different from freshly dissected identified midbrain
166 DA neurons (Puopolo et al., 2007) and thus behave differently from SN DA neurons in slices
167 (Guzman et al., 2009). Nevertheless, our experiments clearly demonstrate that Cav2.3
168 channels contribute to total Ca^{2+}-current and can support pacemaking in cultured mouse DA
169 neurons. This finding requires that Cav2.3 channels must be continuously available throughout
170 the average interspike membrane potentials of these cells (between -70 to -40 mV). However,
171 Cav2.3 α1-subunits have originally been cloned as a low-voltage gated channel with a negative
172 steady-state inactivation voltage range ($V_{0.5,inact}$ -78 mV; Soong et al., 1993) with almost
173 complete inactivation at voltages positive to -50 mV. R-type currents with such negative
174 steady-state inactivation properties have also been described in multiple studies in both native
175 neocortical neurons (Almog & Korngreen, 2009; Sochivko et al., 2002), neurohypophyseal
176 terminals (Wang et al., 1999), cerebellar granule neurons (Randall & Tsien, 1997; Tottene et
177 al., 1996) and recombinant channels co-expressed with α2δ- and various β-subunit isoforms
178 (Jones et al., 1998; Miranda-Laferte et al., 2014; Nakashima et al., 1998; Williams et al., 1994;
179 Yasuda et al., 2004).

180 To explore how Cav2.3 channels can contribute to DA neuron Ca^{2+}-entry during sustained
181 neuronal activity we expressed Cav2.3 α1-subunits together with its accessory α2δ1 and β-
182 subunits in tsA-201 cells under near-physiological conditions. For this purpose we employed
183 physiological extracellular Ca^{2+} (2 mM), weak intracellular Ca^{2+}-buffering (0.5 mM EGTA, see
184 methods), and used AP waveforms recorded from SN DA neurons in mouse midbrain slices
185 (2.5 Hz) or simulated bursts as command voltages as described (Ortner et al., 2017; see
186 methods). Moreover, we employed the Cav2.3e α1-subunit splice variant for our recordings.
187 Among the 6 major Cav2.3 α1-subunit splice variants we only detected Cav2.3e α1 in UV laser-
188 microdissected mouse SN DA neurons in experiments using a qualitative single-cell RT-qPCR
189 approach (Suppl. Fig. 2A,B).

190

191 **β-subunit isoform-dependent activity of Cav2.3 channels during SN DA neuron-like**
192 **regular pacemaking activity**

193 We first employed β3 and β4 isoforms for co-expression experiments in tsA-201 cells, because
194 Cav2 channels in the brain appear to be biochemically associated predominantly with these
195 isoforms (Liu et al., 1996; Scott et al., 1996). When we applied the simulated SN DA neuron
196 regular pacemaker activity (initiated from a holding potential of -89 mV), large inward currents
197 were observed in response to single AP waveforms (Fig. 3A). Cav2.3 channels conducted I_{Ca}
198 during the repolarization phase of the AP (I_{AP}) without evidence for inward current during the
199 interspike interval (ISI, Fig. 3A). However, I_{AP} decreased rapidly during continuous activity and
200 almost completely disappeared after 1 (co-transfected β3) - 2 min (co-transfected β4; Fig. 3B,
201 C). The time course of I_{AP} decrease was best fitted by a bi-exponential function (see legend to
202 Fig. 3). Our data, therefore, suggest that Cav2.3e α1-subunits, in complex with α2δ1 and β3
203 or β4, cannot support substantial inward currents during continuous SN DA neuron
204 pacemaking activity. This is in contrast to our previously published finding of stable Cav1.3
205 Ca^{2+}-channel activity persisting under near identical experimental conditions (Cav1.3
206 α1/α2δ1/β3 previously published data (Ortner et al., 2017) illustrated for comparison in Fig.
207 3B, C). In agreement with earlier studies (Jones et al., 1998; Yasuda et al., 2004), we found
208 that recombinant Cav2.3 channels associated with β3 and β4 inactivate at negative voltages
209 ($V_{0.5,inact}$ < -70 mV) with a rapid inactivation time course (≥ 50% within 50 ms, Fig. 4A-C, Table
210 1). These characteristics can explain the observed rapid loss of Cav2.3 activity during regular
211 pacemaking.

212 Since Cav2.3 channel gating properties have previously been shown to be fine-tuned by β-
213 subunits in an isoform-dependent manner (Jones et al., 1998; Yasuda et al., 2004), we
214 hypothesized that other β-subunits may be required to support long-lasting Cav2.3 activity
215 during firing patterns typical for spontaneously active DA neurons. First, we tested if β-subunits
216 are required at all for Cav2.3 activity under our experimental conditions, as Cav2.3 α1-subunits
217 have been reported to mediate I_{Ca} even when expressed in the absence of β-subunits (Jones
218 et al., 1998; Yasuda et al., 2004). In our experiments, all five tested β-subunits (β2a, β2d, β2e,
219 β3, β4) caused a robust and highly significant (6-12-fold; Fig. 4A, Table 1) increase in current
220 densities with a similar activation voltage-range. This implies that β-associated Cav2.3
221 channels contribute more to overall Cav2.3-mediated currents than channel complexes devoid
222 of β-subunits and thus can be subject to differential modulation by β-subunits. Therefore, we
223 investigated the modulation of Cav2.3 by β2-subunit isoforms, in which N-terminal alternative
224 splicing strongly affects their modulatory effects. In particular, β2a and β2e, which contain N-
225 termini that can anchor to the plasma membrane, can slow the inactivation time course and
226 can affect voltage-dependence of inactivation, especially in Cav2 channels (Jones et al., 1998;
227 Miranda-Laferte et al., 2014; Miranda-Laferte et al., 2012; Yasuda et al., 2004). In contrast, the
228 modulatory effects of other, non-membrane anchored β2 splice variants, such as β2d, are
229 more similar to those of β1, β3 and β4-subunits (Buraei & Yang, 2010). Indeed, also under our

230 experimental conditions β2a and β2e subunits stabilized Cav2.3 voltage-dependent
231 inactivation at ~30 mV more positive potentials compared to β4 (and β3), an effect not
232 observed for β2d subunits (Fig. 4B, Table 1). In contrast, the voltage-dependence of activation
233 was not affected and was similar to β4 and all other tested β-subunits (Fig. 4B, Table 1). β2a
234 and in particular β2e also significantly slowed the inactivation kinetics during prolonged
235 depolarizations compared to all other β-subunits tested (Fig. 4C, Table 1). β3 stabilized
236 significantly faster inactivation kinetics than β4 and β2d subunits. Due to the voltage-
237 dependent inactivation at more depolarized potentials and the resulting overlap of the voltage-
238 dependence of inactivation and activation (Fig. 4B), β2a and β2e subunits induce window
239 currents at negative potentials as shown in Suppl. Fig. 3.

240

241 **β-subunit transcripts in mouse SN and VTA**

242 The above findings prompted us to investigate if β2a and β2e are indeed expressed in SN DA
243 neurons and could, therefore, participate in the formation of R-type currents sustained during
244 pacemaking. We investigated β1-4 subunit expression patterns in the SN (and VTA for
245 comparison) (Fig. 5A) dissected from brain slices of 12-14 weeks old male C57Bl/6N mice (Fig.
246 5C) using a standard curve-based absolute RT-qPCR assay (Schlick et al., 2010; Suppl. Table
247 1). In both SN and VTA tissue β4 (SN: ~65%; VTA: ~56%) and β2 (SN: ~27%; VTA: ~29%)
248 represented the most abundant β-subunit transcripts, followed by β1 and β3 (~5 - 7%) (Fig.
249 5A). Our findings are in excellent agreement (β2: 31-35%, β4: 41-45%) with cell type specific
250 RNA sequencing data from identified midbrain DA neurons (Brichta et al., 2015; Shin, 2015).

251 Next, we used our standard curve-based RT-qPCR assay to specifically quantify β2 N-terminal
252 splice variant transcripts in these brain regions (Fig. 5B; for alignment of N-terminal β2 splice
253 variants see Suppl. Fig. 1A). Assays were designed to specifically discriminate between β2a,
254 β2b, and β2e. β2c and β2d N-termini (also present on other splice variants comprising the β2d
255 N-terminus but with different alternative splicing in the HOOK region; Buraei & Yang, 2010)
256 were detected by a common assay because selective primer design was difficult (see
257 Methods). In SN and VTA, β2a (~30%) and β2e (~26%) transcripts together comprised about
258 half of all tested β2-subunit splice variants, β2c and β2d-species about 42% and β2b only
259 about 3% (Fig. 5B). Therefore, β2a and β2e together should be able to form a substantial
260 fraction of Cav2.3 channel complexes.

261 We further confirmed the presence of the various N-terminal β2 splice variants in individual
262 UV-laser microdissected mouse SN DA neurons at the mRNA level using a qualitative PCR
263 approach (Suppl. Fig. 2C). Moreover, quantitative RNAScope analysis confirmed the

264 expression of both, β2e and β2a variants, in identified mouse SN and VTA DA neurons with
265 β2e more abundantly expressed compared to β2a (Suppl. Fig. 2D).

266

267 **β2 splice variant-dependent regulation of Cav2.3 activity during SN DA neuron-like**
268 **regular pacemaking activity**

269 In order to investigate if the depolarizing shifts in steady-state inactivation and slowing of
270 inactivation kinetics by β2a and β2e subunits are sufficient to stabilize Cav2.3 currents during
271 simulated regular pacemaking activity, we co-expressed these β-subunits with Cav2.3e
272 channels and stimulated cells with the SN DA neuronal AP waveform as described above for
273 β3 or β4 (Fig. 3A). In contrast to β3 or β4, I_{AP} decreased with a much slower time course in the
274 presence of β2a or β2e with about 40% of the maximal initial I_{AP} still remaining even after 5
275 min of continuous activity (Fig. 6A-C). The time course of I_{AP} decrease could be fitted by a bi-
276 exponential function predicting a steady-state reached at 32.3 ± 0.77% (n=12) of the initial I_{AP}
277 for β2a and 25.0 ± 0.12% (n=9) for β2e (see legend to Fig. 6). Similar to co-transfected β3 or
278 β4 subunits, β2a or β2e supported Cav2.3 I_{Ca} predominantly during the repolarization phase
279 after the AP spike. However, in accordance with enhanced window currents at more negative
280 voltages (Suppl. Fig. 3) these subunits also supported an inward current during the interspike
281 interval (ISI) as evident from the first few sweeps (with the largest current amplitudes) (Fig. 6A,
282 bottom panel, zoom-in). I_{AP} persisting after 2 min (β3, β4) or 5 min (β2a, β2e) of pacemaking
283 was completely blocked by 100 µM Cd^{2+} and almost complete recovery from Cd^{2+}-block was
284 observed upon washout (Fig. 6B).

285 Irreversible loss of I_{Ca}, a phenomenon also known as current "run-down" widely described for
286 both native and recombinant Cavs (Kepplinger et al., 2000; Ortner et al., 2017; Schneider et
287 al., 2018) during patch-clamp recordings, may also contribute to the current decay observed
288 during simulated pacemaking. We, therefore, quantified the contribution of current run-down
289 for Cav2.3 co-expressed with α2δ1 and β2a or β3 subunits first by applying short (20 ms)
290 square pulses to V_{max} (hp -89 mV) with a frequency of 0.1 Hz (Fig. 7A). With this protocol (short
291 pulse, long inter-sweep interval, hyperpolarized hp) activity-/voltage-dependent inactivation of
292 Cav2.3 channels should be minimized. While β3 co-transfected Cav2.3 channels showed a
293 time-dependent current run-down after 5 min to about 60% of the peak I_{Ca}, β2a prevented the
294 current decline during this period (Fig. 7A). To further quantify the current run-down during
295 simulated pacemaking we interrupted the pacemaking protocol after different time periods by
296 20 s long pauses at -89 mV to allow channel recovery from inactivation (Fig. 7B). Thus, the
297 percent run-down can be estimated from the non-recovering current component (Fig. 7B,
298 horizontal dashed lines). After 30 s of pacemaking the current amplitude during the first AP
299 after the pause was similar to I_{AP} during the initial AP with both β-subunits (β3: 96.9 ± 3.63%,

95% CI: 86.8-107.0, n=5, N=2; β2a: 107.3 ± 3.66%, 95% CI: 99.3-115.4, n=12, N=2, of the initial I_{AP}). After the pause that followed another 1 min of pacemaking, 83.6 ± 7.33% (95% CI: 63.2-103.9) of the initial current was still recovered with co-transfected β3 but after 2 more minutes of pacemaking recovery decreased to 54.7 ± 6.27% (95% CI: 34.7-74.7, Fig. 7B; ~45% run-down after 4.5 min in total, n=5). This time course is in good agreement with values obtained using the square-pulse protocol (Fig. 7A). Again, run-down was largely prevented by co-expressed β2a-subunits (Fig. 7B; ~16% run-down after 4.5 min in total, n=12).

These data clearly demonstrate that the I_{AP} decrease in response to simulated SN DA neuron pacemaking (2.5 Hz) is almost completely due to the reversible accumulation of Cav2.3 channels in inactivated states, an effect partially prevented by β2a and β2e.

Cav2.3 Ca^{2+} currents during simulated SN DA burst firing activity

In addition to regular pacemaking activity (in vitro) or irregular single spike mode (in vivo), burst firing with transient increases in intracellular Ca^{2+}-load has been associated with neurodegeneration and selective neuronal vulnerability in Parkinson's disease (Dragicevic et al., 2015; Schiemann et al., 2012). Thus, we investigated to which extent Cav2.3 Ca^{2+}-channels can contribute to Ca^{2+}-entry during bursts and after post-burst hyperpolarizing pauses of SN DA neurons. After reaching steady-state I_{AP} during simulated SN DA neuron pacemaking (β4: 1-2 min, β2a/β2e: 5-6 min, see also Fig. 6B) we applied a computer modeled typical three-spike burst, followed by a 1.5 s long afterhyperpolarization-induced pause at more negative potentials as a command voltage as previously described (Ortner et al., 2017) (Fig. 8A). First, we quantified to which extent total burst Ca^{2+}-charge, i.e. I_{Ca} integrated over the duration of the burst, changes as compared to total Ca^{2+}-charge during the same duration of a single AP in steady-state (calculated as the mean of 3 APs preceding the burst). Integrated I_{Ca} during the burst was 4-6-fold higher than the mean integrated I_{Ca} during a steady-state AP with all co-expressed β-subunits (β2a, β2e, β4) (Fig. 8A, B). However, it has to be considered that with co-expressed β4 only ~6% of the initial I_{AP} remained in steady-state during regular pacemaking. Therefore, this relative increase will cause a much smaller rise in absolute Ca^{2+} charge compared to β2a/β2e-associated Cav2.3 where ~40% of I_{AP} persisted in steady-state (Fig. 6B).

We also investigated if post-burst afterhyperpolarizations would allow Cav2.3 channels to recover from inactivation and thus mediate increased Ca^{2+}-entry during the first APs after the burst. We first determined the recovery from inactivation of Cav2.3 channels co-expressed with α2δ1 and β4 or β2a using a square-pulse protocol (Fig. 8C; 1-s conditioning prepulse to V_{max} to inactivate Cav2.3 channels followed by a 10 ms step to V_{max} after different time periods

335 at -89 mV). About 30% of currents recovered under these experimental conditions after 1.5
336 seconds at -89 mV with both co-expressed β4 and β2a (~6-fold increase of the remaining I_{Ca}
337 after 1s at V_{max}). In contrast, recovery during the hyperpolarizing pause after the burst of the
338 AP protocol was much less pronounced (β4) or absent (β2a, β2e) (Fig. 8B). This may be due
339 to the different pulse protocols inducing channel inactivation over different time periods. This
340 may stabilize inactivated states with different recovery times.

341 Taken together, these data predict that β2a- and β2e-associated Cav2.3 channels can
342 contribute to enhanced Ca^{2+}-entry during brief burst activity but not during post-burst APs.

343 Since palmitoylation is reversible and regulated in an activity-dependent localized manner
344 (Bijlmakers & Marsh, 2003; Matt et al., 2019), we also investigated the contribution of
345 palmitoylation of β2a for Cav2.3e modulation under our experimental conditions. To mimic the
346 de-palmitoylated form, we replaced the two N-terminal cysteines to serines ($_{C3S/C4S}$β2a) which
347 prevents plasma membrane anchoring of β2a (Gebhart et al., 2010; Qin et al., 1998). As shown
348 in Suppl. Fig. 4, $_{C3S/C4S}$β2a significantly shifted $V_{0.5,inact}$ of Cav2.3 to more positive voltages as
349 compared to β3 but to a much smaller extent (< 14 mV) than β2a (+35 mV) (Table 1). Due to
350 this prominent role of palmitoylation on the $V_{0.5,inact}$ of Cav2.3 channels, the palmitoylation state
351 of β2a should allow further fine-tuning of non-inactivating current components of Cav2.3
352 channels in SN DA neurons. As illustrated in Suppl. Fig. 4, the effects of β2a palmitoylation on
353 the inactivation kinetics and inactivation voltage of Cav1.3 L-type channels (Suppl. Fig. 4A,C)
354 were different from Cav2.3, suggesting that palmitoylation/depalmitoylation events would
355 regulate Ca^{2+} channel function in a subtype-selective manner.

356

357 **Steady-state activation and inactivation of R-type currents in mouse SN DA neurons**

358 We have recently shown in whole-cell patch-clamp recordings that 100 nM SNX-482 inhibit
359 ~30% of total Cav currents in mouse SN DA neurons (Benkert et al., 2019) when stimulated
360 from a holding potential of -70 mV. If membrane-anchored β2-subunits stabilize more positive
361 $V_{0.5,inact}$ of Cav2.3 channels in SN DA neurons then the voltage-dependent inactivation of the
362 R-type currents should allow channels to be available even at voltages positive to -40 mV.
363 Using whole-cell patch-clamp recordings (Fig. 9), we therefore measured the steady-state
364 inactivation of R-type I_{Ca} in identified SN DA neurons in midbrain slices. R-type current was
365 isolated as the current remaining after preincubation of slices with selective inhibitors of Cav1
366 (1 μM isradipine), Cav2 (Cav2.1, Cav2.2; 1 μM ω-Conotoxin MVIIC) and Cav3 (10 μM Z941))
367 (Fig. 9, blue traces/symbols). The voltage-dependence for steady-state inactivation for R-type
368 I_{Ca} was ~5 mV more positive than for total I_{Ca} ($V_{0.5,inact}$ -52.4 ± 1.58, 95% CI: -55.8 - -49.0 vs -
369 47.5 ± 1.38 mV, 95% CI: -50.5 - -44.6, $p<0.05$; Fig. 9A, Table 3) and very similar to recombinant

370 Cav2.3 currents expressed with α2δ1 plus β2a or β2e subunits (~ -40 mV, Table 1). R-type
371 current evoked from -100 mV activated at about 8 mV more positive voltages than total I_{Ca} (Fig.
372 9A, Table 3 for statistics). This observation is also in accordance with the positive activation
373 voltage range of Cav2.3 channels measured in tsA-201 cells.

374 We independently confirmed the presence of SNX-482-sensitive R-type currents also using
375 perforated patch recordings in identified SN DA neurons. From an even more positive holding
376 potential of -60 mV, where a fraction of Cav2.3 channels must already be inactivated (Fig. 9A),
377 still about 13% of I_{Ca} was inhibited by acute bath application of SNX-482 and inhibition was
378 partially reversible upon washout (Suppl Fig. 5, Suppl. Table 7).

379 These data are consistent with our finding of a contribution of β2a and/or β2e subunits to
380 Cav2.3-mediated R-type current modulation. They also provide the first detailed analysis of
381 Cav2.3-mediated R-type currents in identified SN DA neurons.

382

383 **Discussion**

384 Although the modulation of Cavs by β-subunits and the characteristic gating changes induced
385 by N-terminally membrane-anchored β2-subunit splice variants have been well described in
386 the literature, the physiological significance of these findings remained underexplored. Here
387 we provide strong evidence for an important role of β-subunit alternative splicing for Cav2.3
388 Ca^{2+}-channel signaling during continuous SN DA neuron-like regular pacemaking activity. We
389 show that only β2a and β2e stabilize Cav2.3 channel complexes with voltage-dependent
390 inactivation properties preventing complete inactivation during the on-average depolarized
391 membrane potentials encountered during the pacemaking cycle. This cannot only explain our
392 finding of a substantial contribution of SNX-482-sensitive R-type currents to activity-dependent
393 somatic Ca^{2+}-oscillations in SN DA neurons in brain slices (Benkert et al., 2019) but also to
394 pacemaking frequency in cultured DA neurons. We also provide evidence for the expression
395 of β2a and β2e subunit splice variants in highly vulnerable SN DA and in more resistant VTA
396 DA neurons. Together with our finding that R-type currents in SN DA neurons are available
397 within a voltage range very similar to heterologously expressed β2a- and β2e- stabilized
398 Cav2.3 channel complexes, our data therefore strongly suggest that these subunits are
399 required for normal DA neuron function and may also account for the previously reported
400 pathogenic potential of Cav2.3 Ca^{2+}-channels in PD pathophysiology (Benkert et al., 2019).

401 We have previously shown that Cav2.3-knockout mice are protected from the selective loss of
402 SN DA neurons in the chronic MPTP/probenecid PD model (Benkert et al., 2019). At least in
403 this rodent model of PD, the observed protection provides strong evidence for a role of these
404 channels in PD pathology. Pharmacological inhibition of Cav2.3 alone or together with other
405 Cavs may, therefore, confer beneficial disease-modifying effects and a novel approach for
406 neuroprotection in PD. The recent failure of the L-type Ca^{2+} channel blocker isradipine in the
407 STEADY-PD trial (Parkinson Study Group, 2020) to prevent disease progression in early PD
408 patients indicates that inhibition of L-type channels alone may not be sufficient for
409 neuroprotection. Our previous preclinical findings identifying Cav2.3 channels as novel drug
410 targets for neuroprotective PD-therapy are now supported by demonstrating R-type-mediated
411 I_{Ca} in identified SN DA neurons with voltage-dependent gating properties likely stabilized by
412 Cav2.3 association with β2a and/or β2e. Therefore, the inhibition of Cav2.3 in addition to
413 Cav1.3 may be required for clinically meaningful neuroprotection. However, Cav2.3-mediated
414 R-type currents are notoriously drug-resistant (Schneider et al., 2013), and so far no selective
415 potent small-molecule Cav2.3/R-type blocker has been reported.

416 Our findings reported here now provide the rationale for exploring novel neuroprotective
417 strategies based on Cav2.3 channel inhibition. These could take advantage of the strong
418 dependence of continuous Cav2.3 channel activity on gating properties such as those

419 stabilized by β2a and/or β2e. Rather than inhibiting Ca^{2+}-entry through the pore-forming α1-
420 subunit, such a strategy could aim at reducing its contribution to the R-type current component
421 persisting during continuous activity in SN DA neurons by interfering with the association of
422 β2a and β2e subunits. Even if other β-subunits would replace them in the channel complex
423 and ensure its stable expression, our data suggest that they would not be able to shift the
424 steady-state inactivation voltage into the operating voltage range of SN DA neurons like β2a
425 and β2e. Such an approach appears realistic due to the availability of novel genetically
426 encoded Ca^{2+}-channel inhibitors for a cell-type-specific gene therapeutic intervention. One
427 such approach (CaVablator) has elegantly been used to specifically target Ca^{2+}-channel β-
428 subunits for degradation by fusing β-specific nanobodies with the catalytic HECT domain of
429 Nedd4L, an E3 ubiquitin ligase (Morgenstern et al., 2019). This strongly reduces Cav1- and
430 Cav2-mediated Ca^{2+}-currents in different cell types. At present, it is unclear to which extent
431 other high-voltage activated Cav2 channels (Cav2.1, Cav2.2) also contribute to the high
432 vulnerability of SN DA neurons. However, our recent quantitative RNAScope analyses in
433 mature SN DA neurons (Benkert et al., 2019), clearly demonstrate that Cav2.3 α1-subunit
434 (*Cacna1e*) transcripts are the most abundant α1-subunit expressed in these cells, in excellent
435 agreement with cell type-specific RNAseq data of identified midbrain dopaminergic neurons
436 (Brichta et al., 2015).

437 We also show that in cultured mouse DA neurons, Cav2.3 channels can contribute to
438 pacemaking. SNX-482 is also a potent blocker of Kv4.3 channels (Kimm & Bean, 2014)
439 underlying A-type K^+-currents (I_A). 60 nM nearly fully block reconstituted Kv4.3 currents in HEK
440 cells (IC_{50} ~ 3 nM). Therefore, one can argue that in current-clamp recordings, 50-300 nM
441 SNX-482 could alter pacemaking or the AP shape by effectively blocking Kv4.3 channels.
442 However, our data on spontaneously firing DA neurons show very clearly that 100 nM SNX-
443 482 causes a shortening and a reduced frequency of spontaneous APs, while a block of I_A
444 channels typically induces a broadening of APs in several neuronal preparations (Kim et al.,
445 2005) and an increased frequency in DA neurons (Liss et al., 2001). Therefore, the observed
446 changes induced by SNX-482 strongly argue for a role of non-inactivating Cav2.3-mediated R-
447 type currents for pacemaking in DA neurons in culture.

448 A limitation of our work is that our experiments do not provide direct proof for a role of β2-
449 subunit splice variants for R-type current modulation. Therefore, a similar role of other
450 posttranslational modifications of Cav2.3 channels or protein interaction partners expressed at
451 somatodendritic locations of SN DA neurons (such as Rab3-interacting proteins at axonal
452 sites, Kiyonaka et al., 2007; Robinson et al., 2019) cannot be excluded. Direct proof for a role
453 of β2-subunit splice variants would require a splice-variant-specific gene knockout or siRNA-
454 mediated knock-down of both β2a and β2e subunits in SN DA neurons, followed by isolation
455 of Cav2.3 current components which is methodologically challenging in these neurons.

456 Nevertheless, we provide the first example for a physiological and perhaps even
457 pathophysiological role of β2-subunit alternative splicing emphasizing a need for further
458 investigation in other types of neurons.

459

460 **Materials and Methods**

461 **Animals**

462 For quantitative real-time PCR (RT-qPCR) experiments, male C57BL/6N mice were bred in
463 the animal facility of the Centre for Chemistry and Biomedicine (CCB) of the University of
464 Innsbruck (approved by the Austrian Animal Experimentation Ethics Board). For
465 electrophysiological experiments of cultured midbrain DA neurons, C57Bl/6 TH-GFP mice
466 (Matsushita et al., 2002; Sawamoto et al., 2001) were kept heterozygous via breeding them
467 with C57Bl/6 mice (in accordance with the European Community's Council Directive
468 2010/63/UE and approved by the Italian Ministry of Health and the Local Organism responsible
469 for animal welfare at the University of Torino; authorization DGSAF 0011710-P-26/07/2017).
470 All animals were housed under a 12 hours light/dark cycle with food and water ad libitum. For
471 whole cell voltage-clamp recordings of SN DA neurons in acute brain slices, as well as single-
472 cell RT-qPCR, juvenile male C57Bl/6 mice (PN11-13) were bred at the animal facility of Ulm
473 University. For RNAScope analysis, adult male C57Bl/6 mice and Cav2.3 WT mice were bred
474 at the animal facility of Ulm University. Animal procedures at the Universities of Ulm
475 (Regierungspräsidium Tübingen, Ref: 35/9185.81-3; Reg. Nr. o.147) and Cologne (LANUV
476 NRW, Recklinghausen, Germany (84-02.05.20.12.254) were approved by the local authorities.

477 **RNA isolation and cDNA synthesis for tissue RT-qPCR**

478 Tissue was dissected after mice had been sacrificed by cervical dislocation under isoflurane
479 (Vetflurane, Vibac UK, 1000 mg/g) anesthesia and RNA isolation and cDNA synthesis for
480 tissue RT-qPCR was performed as described in Supplemental Methods.

481 **Quantitative RT-qPCR of mouse brain tissue samples**

482 Fragments of β-subunits and β2 splice variants were amplified from mouse whole brain cDNA
483 utilizing specific primers (Suppl. Table 1) and subcloned into the Cav1.3 8a 42 pGFP^{minus} vector
484 after restriction enzyme digestion using SalI and HindIII. Primer sequences for β1-β4 have
485 been described previously (Schlick et al., 2010), but additional SalI and HindIII restriction
486 enzyme sites (underlined in Suppl. Table 1) were inserted to allow subsequent ligation of
487 fragments into the digested vector. TaqMan gene expression assays (Thermo Fisher Scientific,
488 Waltham, MA, USA) and custom-made TaqMan gene expression assays were designed to

489 span exon-exon boundaries (Suppl. Table 1) as already described (Nadine J. Ortner et al.,
490 2020).

491 The expression of β1, β2, β3, β4, β2a, β2b, β2c-d, and β2e was assessed using a standard
492 curve method-based on PCR fragments of known concentration (Nadine J. Ortner et al., 2020;
493 Schlick et al., 2010). β2c and β2d were detected by a common assay as selective primer
494 design failed due to high sequence similarity. This assay binds at the exon-exon boundary of
495 exons 2A and 3 of β2c and β2d and also recognizes a number of splice variants comprising
496 the β2d N-terminus but with different alternative splicing in the HOOK region of the subunit
497 (Buraei & Yang, 2010). Details about assay specificity are given in Suppl. Fig.1.

498 **cDNA constructs**

499 For transient transfections hCav2.3e (cloned into pcDNA3, Pereverzev et al., 2002) or
500 hCav1.3$_L$ (human C-terminally long Cav1.3 splice variant; GenBank accession number
501 EU363339) α1 subunits were transfected together with the previously described accessory
502 subunit constructs: β3 (rat, NM_012828, Koschak et al., 2001), β2a (rat, M80545, Koschak et
503 al., 2001), β2d (mouse, β2aN1, FM872408.1; Link et al., 2009), β2e (mouse, β2aN5,
504 FM872407; Link et al., 2009, where β2d and β2e were kindly provided by V. Flockerzi,
505 Saarland University, Homburg), $_{C3S/C4S}$β2a (cysteine residues in position 3 and 4 of β2a
506 replaced by serines, Gebhart et al., 2010) or β4 (rat, splice variant β4e, kindly provided by Dr.
507 Bernhard Flucher, Medical University Innsbruck; Etemad et al., 2014) and α2δ1 (rabbit,
508 NM_001082276, Koschak et al., 2001).

509 **Cell culture and transfection**

510 TsA-201 cells (European Collection of Cell Culture, catalog #96121229) were cultured as
511 described (N. J. Ortner et al., 2020) in Dulbecco's modified Eagle's medium (DMEM; Sigma-
512 Aldrich, catalog #D6546) that was supplemented with 10% fetal bovine serum (FBS, Gibco,
513 catalog #10270-106), 2 mM L-glutamine (Gibco, catalog #25030-032), penicillin (10 units/ml,
514 Sigma, P-3032) and streptomycin (10 µg/ml, Sigma, S-6501). Cells were maintained at 37°C
515 and 5% CO_2 in a humidified incubator and were subjected to a splitting procedure after
516 reaching ~80% confluency. For splitting, cells were dissociated using 0.05% trypsin after
517 implementing a washing step using 1 x phosphate buffered saline (PBS). TsA-201 cells were
518 replaced and freshly thawed when they exceeded passage no. 21. For electrophysiology, cells
519 were plated on 10-cm culture dishes and subjected to transient transfections on the following
520 day. Cells were transiently transfected using Ca^{2+}-phosphate as previously described (Ortner
521 et al., 2014) with 3 µg of α1 subunits, 2 µg of β subunits, 2.5 µg of α2δ1 subunits and 1.5 µg
522 of eGFP to visualize transfected cells. On the next day, cells were plated onto 35-mm culture

523 dishes that were coated with poly-L-lysine, kept at 30°C and 5% CO_2 and were then subjected
524 to whole-cell patch-clamp experiments after 24-72 hours.

525 **Primary cell culture of midbrain DA neurons**

526 As described in Tomagra et al., 2019, the methods for the primary culture of mesencephalic
527 dopamine neurons from substantia nigra (SN) were adapted from Pruszak et al., 2009. Briefly,
528 the ventral mesencephalon area was dissected from embryonic (E15) C57Bl/6 TH-GFP mice
529 (Matsushita et al., 2002; Sawamoto et al., 2001) that were kept heterozygous via breeding
530 them with C57Bl/6J mice. HBSS (Hank's balanced salt solution, without $CaCl_2$ and $MgCl_2$),
531 enriched with 0.18% glucose, 1% BSA, 60% papain (Worthington, Lakewood, NJ, United
532 States), 20% DNase (Sigma-Aldrich) was stored at 4°C and used as digestion buffer. Neurons
533 were plated at final densities of 600 cells per mm^2 on Petri dishes. Cultured neurons were used
534 at 8/9 days in vitro (DIV) for current-clamp and voltage-clamp experiments. Petri dishes were
535 coated with poly-L-Lysine (0.1 mg/ml) as substrate adhesion. Cells were incubated at 37°C in
536 a 5% CO_2 atmosphere, with Neurobasal Medium containing 1% pen-strep, 1% ultra-glutamine,
537 2% B-27, and 2.5% FBS dialyzed (pH 7.4) (as previously described in Tomagra et al., 2019).

538 **Whole-cell patch-clamp recordings in tsA-201 cells**

539 For whole-cell patch-clamp recordings, patch pipettes with a resistance of 1.5-3.5 MΩ were
540 pulled from glass capillaries (Borosilicate glass, catalog #64-0792, Harvard Apparatus, USA)
541 using a micropipette puller (Sutter Instruments) and fire-polished with a MF-830 microforge
542 (Narishige, Japan). Recordings were obtained in the whole-cell configuration using an
543 Axopatch 200B amplifier (Axon Instruments, Foster City, CA), digitized (Digidata 1322A
544 digitizer, Axon Instruments) at 50 kHz, low-pass filtered at 5 kHz and subsequently analyzed
545 using Clampfit 10.7 Software (Molecular Devices). Linear leak and capacitive currents were
546 subtracted online using the P/4 protocol (20ms I-V protocol) or offline using a 50 ms
547 hyperpolarizing voltage step from -89 to -99 mV or -119 to -129 mV. All voltages were corrected
548 for a liquid junction potential (JP) of -9 mV (Lieb et al., 2014). Compensation was applied for
549 70-90% of the series resistance.

550 The pipette internal solution for recordings of Cav2.3 contained (in mM): 144.5 CsCl, 10
551 HEPES, 0.5 Cs-EGTA, 1 $MgCl_2$, 4 Na_2ATP adjusted to pH 7.4 with CsOH (299 mOsm/kg). The
552 pipette internal solution for recordings of Cav1.3 contained (in mM): 135 CsCl, 10 HEPES, 10
553 Cs-EGTA, 1 $MgCl_2$, 4 Na_2ATP adjusted to pH 7.4 with CsOH (275 mOsm/kg). The bath solution
554 for recordings of Cav2.3 contained (in mM): 2 $CaCl_2$, 10 HEPES, 170 Choline-Cl and 1 $MgCl_2$
555 adjusted to pH 7.4 with CsOH. The bath solution for recordings of Cav1.3 contained (in mM):
556 15 $CaCl_2$, 10 HEPES, 150 Choline-Cl and 1 $MgCl_2$ adjusted to pH 7.4 with CsOH.

557 Current-voltage (I-V) relationships were obtained by applying a 20 ms long square pulse
558 protocol to various test potentials (5 mV voltage steps) starting from a holding potential (hp) of
559 -119 mV or -89 mV (recovery of inactivation). The resulting I-V curves were fitted to the
560 following equation:

561 $$I = G_{max}(V - V_{rev})/(1 + \exp\left[-\frac{V - V_{0.5}}{k}\right]),$$

562 where I is the peak current amplitude, G_{max} is the maximum conductance, V is the test potential,
563 V_{rev} is the extrapolated reversal potential, $V_{0.5}$ is the half-maximal activation voltage, and k is
564 the slope factor. The voltage dependence of Ca^{2+}-conductance was fitted using the following
565 Boltzmann relationship:

566 $$G = G_{max}/(1 + \exp\left[-\frac{V - V_{0.5}}{k}\right])$$

567 The voltage dependence of inactivation was assessed by application of 20 ms test pulses to
568 the voltage of maximal activation (V_{max}) before ($I_{control}$) and after holding the cell at various
569 conditioning test potentials for 5 s (30 s inter-sweep interval; 10 mV voltage steps; hp -119
570 mV). Inactivation was calculated as the ratio between the current amplitudes of the 20 ms test
571 pulses. Steady-state inactivation parameters were obtained by fitting the data to a modified
572 Boltzmann equation:

573 $$I = (1 - I_{control})/(1 + \exp\left[\frac{V - V_{0.5,\ inact}}{k_{inact}}\right] + I_{control}),$$

574 where $V_{0.5,\ inact}$ is the half-maximal inactivation voltage, and k_{inact} is the inactivation slope factor.

575 The amount of inactivation during a 5 s depolarizing pulse from a hp of -119 mV to the V_{max}
576 was quantified by calculating the remaining current fraction after 50, 100, 250, 500, 1000 and
577 5000 ms. Recovery from inactivation was determined by 10 ms test pulses to V_{max} at different
578 time-points (in s: 0.001, 0.003, 0.01, 0.03, 0.1, 0.3, 0.6, 1, 1.5, 2, 3, 4, 6, 8, 10, 15, 20) after a
579 1-s conditioning pulse to V_{max} (hp -89 mV). Window current was determined by multiplying
580 mean current densities by fractional currents form steady-state inactivation curves to obtain
581 the fraction of available channels at a given potential as described previously (Hofer et al.,
582 2020). The SN DA regular pacemaking command voltage protocol obtained from an identified
583 TH^+ SN DA neuron in a mouse brain slice (male, P12) and the SN DA burst firing protocol were
584 generated as previously described (Ortner et al., 2017). Cells were perfused by an air
585 pressure-driven perfusion system (BPS-8 Valve Control System, ALA Scientific Instruments)
586 with bath solution and a flow rate of 0.6 ml/min. For Cd^{2+}-block, cells were perfused with 100
587 µM Cd^{2+} to achieve full block, followed by wash-out with bath solution. A complete exchange
588 of the solution around the cell was achieved within <50 ms. All experiments were performed at
589 room temperature (~22°C).

590 **Voltage- and current-clamp recordings in cultured midbrain DA neurons**

591 Macroscopic whole-cell currents and APs were recorded using an EPC 10 USB HEKA amplifier
592 and Patchmaster software (HEKA Elektronik GmbH) following the procedures described
593 previously (Baldelli et al., 2005; Gavello et al., 2018). Traces were sampled at 10 kHz and
594 filtered using a low-pass Bessel filter set at 2 kHz. Borosilicate glass pipettes (Kimble Chase
595 life science, Vineland, NJ, USA) with a resistance of 7-8 MΩ were used. Uncompensated
596 capacitive currents were reduced by subtracting the averaged currents in response to P/4
597 hyperpolarizing pulses. Off-line data analysis was performed with pClamp 10.0 software for
598 current clamp recordings. Ca^{2+} currents were evoked by applying a single depolarization step
599 (50 ms duration), from a holding of -70 mV to 0 mV. Fast capacitive transients due to the
600 depolarizing pulse were minimized online by the patch-clamp analog compensation. Series
601 resistance was compensated by 80% and monitored during the experiment.

602 For current-clamp experiments the pipette internal solution contained in mM: 135 gluconic acid
603 (potassium salt: K-gluconate), 10 HEPES, 0.5 EGTA, 2 $MgCl_2$, 5 NaCl, 2 ATP-Tris and 0.4
604 Tris-GTP (Tomagra et al., 2019). For voltage-clamp recordings the pipette internal solution
605 contained in mM: 90 CsCl, 20 TEA-Cl, 10 EGTA, 10 glucose, 1 $MgCl_2$, 4 ATP, 0.5 GTP and 15
606 phosphocreatine adjusted to pH 7.4. The extracellular solution for current/voltage-clamp
607 recordings (Tyrode's solution) contained in mM: 2 $CaCl_2$, 10 HEPES, 130 NaCl, 4 KCl, 2 $MgCl_2$,
608 10 glucose adjusted to pH 7.4. Patch-clamp experiments were performed using pClamp
609 software (Molecular Devices, Silicon Valley, CA, United States). All experiments were
610 performed at a temperature of 22–24°C. Data analysis was performed using Clampfit software.
611 To study the contribution of Cav2.3 channels to the total Ca^{2+} current, cells were perfused with
612 recording solution (containing in mM: 135 TEA, 2 $CaCl_2$, 2 $MgCl_2$, 10 HEPES, 10 glucose
613 adjusted to pH 7.4) complemented with 300 nM TTX and 3 μM ISR to block voltage-dependent
614 Na^+ and L-type Ca^{2+} channels. SNX-482 (100 nM) was used in current- and voltage-clamp
615 experiments. Furthermore, kynurenic acid (1 mM), 6,7-dinitroquinoxaline-2,3-dione (DNQX)
616 (20 μM) and picrotoxin (100 μM) were present in the extracellular solution for current- and
617 voltage-clamp experiments.

618 **Whole cell voltage-clamp recordings of SN DA neurons in acute brain slices**

619 Whole-cell patch-clamp recordings were performed essentially as previously described
620 (Benkert et al., 2019). In brief, murine (PN11-13) coronal midbrain slices were prepared in ice-
621 cold ACSF using a VibrosliceTM (Campden Instruments). Chemicals were obtained from
622 Sigma Aldrich unless stated otherwise. ACSF contained in mM: 125 NaCl, 25 $NaHCO_3$, 2.5
623 KCl, 1.25 NaH_2PO_4, 2 $CaCl_2$, 2 $MgCl_2$ and 25 glucose, and was gassed with Carbogen (95%
624 O_2, 5% CO_2, pH 7.4, osmolarity was 300 - 310 mOsm/kg). Slices were allowed to recover for
625 30 min at room temperature (22-25°C) before use for electrophysiology. Recordings were

626 carried out in a modified ACSF solution containing in mM: 125 NaCl, 25 $NaHCO_3$, 2.5 KCl,
627 1.25 NaH_2PO_4, 2.058 $MgCl_2$, 1.8 $CaCl_2$, 2.5 glucose, 5 CsCl, 15 tetraethylammonium, 2.5 4-
628 aminopyridine, 600 nM TTX (Tocris), 20 µM CNQX (Tocris), 4 µM SR 95531 (Tocris) and 10
629 µM DL-AP5 (Tocris), pH adjusted to 7.4, osmolarity was 300 - 315 mOsm/kg. Data were
630 digitalised with 2 kHz, and filtered with Bessel Filter 1: 10 kHz; Bessel Filter 2: 5 kHz. All
631 recordings were performed at a bath temperature of 33°C ± 1. Patch pipettes (2.5-3.5 MΩ)
632 were filled with internal solution containing in mM: 180 N-Methyl-D-glucamine, 40 HEPES, 0.1
633 EGTA, 4 $MgCl_2$, 5 Na-ATP, 1 Lithium-GTP, 0.1% neurobiotin tracer (Vector Laboratories); pH
634 was adjusted to 7.35 with H_2SO_4, osmolarity was 285 - 295 mOsm/kg. Neurons were filled with
635 neurobiotin during the recording, fixed with a 4% PFA solution and stained for tyrosine
636 hydroxylase (TH; rabbit anti-TH, 1:1000, Cat#: 657012, Merck Millipore) and neurobiotin
637 (Streptavidin Alexa Fluor conjugate 647, 1:1000, Cat# S21374, Thermo Fisher Scientific). Only
638 TH and neurobiotin positive cells were used for the statistical analysis.

639 Steady-state activation was measured by applying 150 ms depolarizing square pulses to
640 various test potentials (10 mV increments) starting from -90 mV with a 10 sec interpulse
641 interval. Holding potential between the pulses was −100 mV. Voltage at maximal Ca^{2+} current
642 amplitude (V_{max}) was determined during the steady-state activation recordings. Voltage-
643 dependence of the steady-state inactivation was measured by applying a 20 ms control test
644 pulse (from holding potential -100 mV to V_{max}) followed by 5 s conditioning steps to various
645 potentials (10 mV increments) and a subsequent 20 ms test pulse to V_{max} with a 10 sec
646 interpulse interval. Inactivation was calculated as the ratio between the current amplitudes of
647 the test versus control pulse. Currents were leak subtracted on-line using the P/4 subtraction.
648 The series resistance was compensated by 60-90%. Data were not corrected for liquid junction
649 potential (-5 mV, measured according to Neher, 1992). Midbrain slices were preincubated
650 (bad-perfusion) at least 30 min in T-type (10 µM Z941), L-type (1 µM isradipine, ISR), N- and
651 P/Q-type (1 µM ω-conotoxin-MVIIC) or R-type (100 nM SNX-482) Ca^{2+} channel blockers;
652 except Z941, which was kindly obtained from T. Snutch (University of British Columbia,
653 Canada), all Cav Blocker were from Tocris.

654 Steady-state activation and inactivation curves were fitted as described above.

655 **Perforated patch recordings in SN DA neurons**

656 Brain slice preparation was performed as described in Supplemental Methods. After
657 preparation, brain slices were transferred to a recording chamber (~1.5 ml volume) and initially
658 superfused with carbogenated ACSF at a flow rate of ~2 ml/min. During the perforation
659 process, the electrophysiological identification of the neuron was performed in current clamp
660 mode. Afterwards, the ACSF was exchanged for the Ca^{2+} current recording solution which
661 contained in mM: 66.5 NaCl, 2 $MgCl_2$, 3 $CaCl_2$, 21 $NaHCO_3$, 10 HEPES, 5 Glucose adjusted

662 to pH 7.2 (with HCl). Sodium currents were blocked by 1 µM tetrodotoxin (TTX). Potassium
663 currents and the hyperpolarization-activated cyclic nucleotide-gated cation current (I_h) were
664 blocked by: 40 mM TEA-Cl, 0.4 mM 4-AP, 1 µM M phrixotoxin-2 (Alomone, Cat # STP-710;
665 Subramaniam et al., 2014) and 20 mM CsCl. Experiments were carried out at ~28°C.
666 Recordings were performed with an EPC10 amplifier (HEKA, Lambrecht, Germany) controlled
667 by the software PatchMaster (version 2.32; HEKA). In parallel, data were sampled at 10 kHz
668 with a CED 1401 using Spike2 (version 7) (both Cambridge Electronic Design, UK) and low-
669 pass filtered at 2 kHz with a four-pole Bessel filter**.** The liquid junction potential between
670 intracellular and extracellular solution was compensated (12 mV; calculated with Patcher's
671 Power Tools plug-in for Igor Pro 6 (Wavemetrics, Portland, OR, USA)).

672 Perforated patch recordings were performed using protocols modified from (Horn & Marty,
673 1988) and (Akaike & Harata, 1994). Electrodes with tip resistances between 2 and 4 MΩ were
674 fashioned from borosilicate glass (0.86 mm inner diameter; 1.5 mm outer diameter; GB150-
675 8P; Science Products) with a vertical pipette puller (PP-830; Narishige, London, UK). Patch
676 recordings were performed with ATP and GTP free pipette solution containing (in mM): 138
677 Cs-methanesulfonate, 10 $CsCl_2$, 2 $MgCl_2$, 10 HEPES and adjusted to pH 7.2 (with CsOH). ATP
678 and GTP were omitted from the intracellular solution to prevent uncontrolled permeabilization
679 of the cell membrane (Lindau & Fernandez, 1986). The patch pipette was tip filled with internal
680 solution and back filled with 0.02% tetraethylrhodamine-dextran (D3308, Invitrogen, Eugene,
681 OR, USA) and amphotericin-containing internal solution (~400 µg/ml; G4888; Sigma-Aldrich,
682 Taufkirchen, Germany) to achieve perforated patch recordings. Amphotericin was dissolved in
683 dimethyl sulfoxide (final concentration: 0.2 - 0.4%; DMSO; D8418, Sigma-Aldrich) (Rae et al.,
684 1991), and was added to the modified pipette solution shortly before use. The used DMSO
685 concentration had no obvious effect on the investigated neurons. During the recordings access
686 resistance (R_a) was constantly monitored and experiments were started after R_a was < 20MΩ.
687 In the analyzed recordings R_a was comparable, did not change significantly over recording
688 time, and was not significantly different between the distinct experimental groups. A change to
689 the whole-cell configuration was indicated by a sudden change in R_a and diffusion of
690 tetraethylrhodamine-dextran into the neuron. Such experiments were rejected. GABAergic and
691 glutamatergic synaptic input was reduced by addition of 0.4 mM picrotoxin (P1675; Sigma-
692 Aldrich), 50 µM D-AP5 (A5282; Sigma-Aldrich), and 10 µM CNQX (C127; Sigma-Aldrich) to
693 the ACSF. For inhibition experiments, 100 nM SNX-482 (Alomone, Cat # RTS-500 dissolved
694 in ACSF) or 10 µM nifedipine (Alomone, Cat # N-120 diluted into ACSF from a freshly prepared
695 10 mM stock solution in DMSO) was bath applied (in ACSF).

696 **Identification of β-subunit transcripts in identified SN DA and VTA DA neurons**

697 **RNAScope *in situ* hybridization**

698 *In situ* hybridization experiments were performed on fresh frozen mouse brain tissue using the
699 RNAScope® technology (Advanced Cell Diagnostics, ACD), according to the manufacturer's
700 protocol under RNase-free conditions and essentially as described (Benkert et al., 2019).
701 Briefly, 12 µm coronal cryosections were prepared (Duda et al., 2018), mounted on
702 SuperFrost® Plus glass slides, and dried for one hour at -20°C. Directly before starting the
703 RNAScope procedure, sections were fixed with 4% PFA for 15 min at 4°C and dehydrated
704 using an increasing ethanol series (50%, 75%, 100%, 100%), for 5 min each. After treatment
705 with protease IV (ACD, Cat# 322336) for 30 min at room temperature, sections were hybridized
706 with the respective target probes for 2 h at 40°C in a HybEZ II hybridization oven (ACD). Target
707 probe signals were amplified using the RNAScope Fluorescent Multiplex Detection Kit (ACD,
708 Cat# 320851). All amplifier solutions were dropped on respective sections, incubated at 40°C
709 in the HybEZ hybridization oven, and washed twice with wash buffer (ACD) between each
710 amplification step for 2 min each. Nuclei were counterstained with DAPI ready-to-use solution
711 (ACD, included in Kit) and slides were coverslipped with HardSet mounting medium
712 (VectaShield, Cat# H-1400) and dried overnight. Target probes were either obtained from the
713 library of validated probes provided by Advanced Cell Diagnostics (ACD) or self-designed in
714 cooperation with ACD. Target probes and image acquisition are described in Supplemental
715 Methods.

716 **Multiplex-nested PCR, qualitative and quantitative PCR analysis in individual laser-**
717 **microdissected DA neurons**

718 Cryosectioning, UV-laser microdissection (UV-LMD) and reverse transcription as well as
719 multiplex-nested PCR, qualitative and quantitative PCR analysis were carried out similarly as
720 previously described in detail (Benkert et al., 2019; Duda et al., 2018; Grundemann et al., 2011;
721 Simons et al., 2019). All cDNA samples were precipitated prior to PCR, as described (Liss,
722 2002). More details are given in Supplemental Methods.

723 **Statistics**

724 Data were analyzed using Clampfit 10.7 (Axon Instruments), Microsoft Excel, SigmaPlot 14.0
725 (Systat Software, Inc), and GraphPad Prism 5 or 7.04 software (GraphPad software, Inc). Data
726 were analyzed by appropriate statistical testing as indicated in detail for all experiments in the
727 text, figure and table legends. Statistical significance was set at $p < 0.05$. Brain slice patch-
728 clamp data were also analyzed with FitMaster (v2x90.5, HEKA Elektronik). RNAScope and
729 single-cell RT-qPCR data data were analyzed by Fiji (https://imagej.net/Fiji), QuantStudio™
730 Design and Analysis Software (Applied Biosystems) and GraphPad Prism 7.04. All values are
731 presented as mean ± SEM (95% confidence interval) for the indicated number of experiments
732 (n) from N independent experiments (biological replications) in the text and Figures unless
733 stated otherwise.

734

735 **Acknowledgements**

736 This work was supported by the Austrian Science Fund (FWF, P27809, W1101, CavX-DOC
737 30 doc.fund) and the Tyrolean Science Fund (TWF, UNI-0404/2345), by the Italian Miur
738 (2015FNWP34) and by the Compagnia di San Paolo (CSTO165284). We thank Dr. Veit
739 Flockerzi for cDNA of β2 splice variants, and Jennifer Müller and Gospava Stojanovic for expert
740 technical assistance.

741

742 **Author Contributions Statement**

743 JS, NJO, and AS designed the study, AS performed electrophysiological recordings in tsA-201
744 cells, EMF dissected SN and VTA tissue, NTH prepared cDNA from mouse tissue, NTH and
745 KV performed RT-qPCR analyses, NW performed RNAScope experiments, JB, JD performed
746 SN DA neuron Cav2.3 splice variant analysis, JD, DS performed UV-LMD and single-cell RT-
747 qPCR, AG, CP performed whole cell patch clamp recordings of SN DA neurons from acute
748 mouse brain slices; GT performed electrophysiological recordings and VC and EC designed,
749 analyzed and interpreted the experiments of AP and Cav current recordings in cultured
750 neurons; PK and SH performed recordings in SN DA neurons in slices, JS, NJO and AS
751 prepared the manuscript and all authors reviewed and revised the final manuscript.

752

753 **Competing interests**

754 The authors declare that they have no financial and non-financial competing interests.

755 **References**

756 Akaike, N., & Harata, N. (1994). Nystatin perforated patch recording and its applications to analyses
757 of intracellular mechanisms. *Jpn J Physiol*, *44*(5), 433-473.
758 https://doi.org/10.2170/jjphysiol.44.433
759 Almog, M., & Korngreen, A. (2009). Characterization of voltage-gated Ca(2+) conductances in layer 5
760 neocortical pyramidal neurons from rats. *PLoS One*, *4*(4), e4841.
761 https://doi.org/10.1371/journal.pone.0004841
762 Baldelli, P., Hernandez-Guijo, J. M., Carabelli, V., & Carbone, E. (2005). Brain-derived neurotrophic
763 factor enhances GABA release probability and nonuniform distribution of N- and P/Q-type
764 channels on release sites of hippocampal inhibitory synapses. *J Neurosci*, *25*(13), 3358-3368.
765 https://doi.org/10.1523/JNEUROSCI.4227-04.2005
766 Benkert, J., Hess, S., Roy, S., Beccano-Kelly, D., Wiederspohn, N., Duda, J., Simons, C., Patil, K.,
767 Gaifullina, A., Mannal, N., Dragicevic, E., Spaich, D., Müller, S., Nemeth, J., Hollmann, H.,
768 Deuter, N., Mousba, Y., Kubisch, C., Poetschke, C., Striessnig, J., Pongs, O., Schneider, T.,
769 Wade-Martins, R., Patel, S., Parlato, R., Frank, T., Kloppenburg, P., & Liss, B. (2019). Cav2.3
770 channels contribute to dopaminergic neuron loss in a model of Parkinson's disease. *Nature*
771 *Communications*, *10*(1), 5094. https://doi.org/10.1038/s41467-019-12834-x
772 Biglan, K. M., Oakes, D., Lang, A. E., Hauser, R. A., Hodgeman, K., Greco, B., Lowell, J., Rockhill, R.,
773 Shoulson, I., Venuto, C., Young, D., Simuni, T., & Investigators, P. S. G. S. P. I. (2017). A novel
774 design of a Phase III trial of isradipine in early Parkinson disease (STEADY-PD III). *Ann Clin*
775 *Transl Neurol*, *4*, 360-368. https://doi.org/10.1002/acn3.412
776 Bijlmakers, M. J., & Marsh, M. (2003). The on-off story of protein palmitoylation. *Trends Cell Biol*,
777 *13*(1), 32-42.
778 Bock, G., Gebhart, M., Scharinger, A., Jangsangthong, W., Busquet, P., Poggiani, C., Sartori, S.,
779 Mangoni, M. E., Sinnegger-Brauns, M. J., Herzig, S., Striessnig, J., & Koschak, A. (2011).
780 Functional properties of a newly identified C-terminal splice variant of Cav1.3 L-type Ca^{2+}
781 channels [Research Support, N.I.H., Extramural

782 Research Support, Non-U.S. Gov't]. *J Biol Chem*, *286*(49), 42736-42748.
783 https://doi.org/10.1074/jbc.M111.269951
784 Bolam, J. P., & Pissadaki, E. K. (2012). Living on the edge with too many mouths to feed: why
785 dopamine neurons die. *Mov Disord*, *27*, 1478-1483. https://doi.org/10.1002/mds.25135
786 Bourinet, E., Stotz, S. C., Spaetgens, R. L., Dayanithi, G., Lemos, J., Nargeot, J., & Zamponi, G. W.
787 (2001). Interaction of SNX482 with domains III and IV inhibits activation gating of alpha(1E)
788 (Ca(V)2.3) calcium channels. *Biophys J*, *81*(1), 79-88. https://doi.org/10.1016/s0006-
789 3495(01)75681-0

790 Branch, S. Y., Sharma, R., & Beckstead, M. J. (2014). Aging decreases L-type calcium channel currents
791 and pacemaker firing fidelity in substantia nigra dopamine neurons. *J Neurosci*, *34*, 9310-
792 9318. https://doi.org/10.1523/JNEUROSCI.4228-13.2014
793 Brichta, L., Shin, W., Jackson-Lewis, V., Blesa, J., Yap, E. L., Walker, Z., Zhang, J., Roussarie, J. P.,
794 Alvarez, M. J., Califano, A., Przedborski, S., & Greengard, P. (2015). Identification of
795 neurodegenerative factors using translatome-regulatory network analysis. *Nat Neurosci*,
796 *18*(9), 1325-1333. https://doi.org/10.1038/nn.4070
797 Buraei, Z., & Yang, J. (2010). The ß subunit of voltage-gated Ca^{2+} channels. *Physiol Rev*, *90*(4), 1461-
798 1506. https://doi.org/10.1152/physrev.00057.2009
799 Burbulla, L. F., Song, P., Mazzulli, J. R., Zampese, E., Wong, Y. C., Jeon, S., Santos, D. P., Blanz, J.,
800 Obermaier, C. D., Strojny, C., Savas, J. N., Kiskinis, E., Zhuang, X., Kruger, R., Surmeier, D. J., &
801 Krainc, D. (2017). Dopamine oxidation mediates mitochondrial and lysosomal dysfunction in
802 Parkinson's disease. *Science*, *357*(6357), 1255-1261.
803 https://doi.org/10.1126/science.aam9080
804 Damier, P., Hirsch, E. C., Agid, Y., & Graybiel, A. M. (1999). The substantia nigra of the human brain. II.
805 Patterns of loss of dopamine-containing neurons in Parkinson's disease. *Brain*, *122 (Pt 8)*,
806 1437-1448. http://www.ncbi.nlm.nih.gov/pubmed/10430830
807 Dragicevic, E., Schiemann, J., & Liss, B. (2015). Dopamine midbrain neurons in health and Parkinson's
808 disease: Emerging roles of voltage-gated calcium channels and ATP-sensitive potassium
809 channels. *Neuroscience*, *284*, 798-814. https://doi.org/10.1016/j.neuroscience.2014.10.037
810 Duda, J., Fauler, M., Grundemann, J., & Liss, B. (2018). Cell-Specific RNA Quantification in Human SN
811 DA Neurons from Heterogeneous Post-mortem Midbrain Samples by UV-Laser
812 Microdissection and RT-qPCR. *Methods Mol Biol*, *1723*, 335-360.
813 https://doi.org/10.1007/978-1-4939-7558-7_19
814 Etemad, S., Obermair, G. J., Bindreither, D., Benedetti, A., Stanika, R., Di Biase, V., Burtscher, V.,
815 Koschak, A., Kofler, R., Geley, S., Wille, A., Lusser, A., Flockerzi, V., & Flucher, B. E. (2014).
816 Differential neuronal targeting of a new and two known calcium channel β4 subunit splice
817 variants correlates with their regulation of gene expression. *The Journal of Neuroscience: The*
818 *Official Journal of the Society for Neuroscience*, *34*, 1446-1461.
819 https://doi.org/10.1523/JNEUROSCI.3935-13.2014
820 Evans, R. C., Zhu, M., & Khaliq, Z. M. (2017). Dopamine Inhibition Differentially Controls Excitability of
821 Substantia Nigra Dopamine Neuron Subpopulations through T-Type Calcium Channels. *J*
822 *Neurosci*, *37*(13), 3704-3720. https://doi.org/10.1523/JNEUROSCI.0117-17.2017

823 Gantz, S. C., Ford, C. P., Morikawa, H., & Williams, J. T. (2018). The Evolving Understanding of
824 Dopamine Neurons in the Substantia Nigra and Ventral Tegmental Area. *Annu Rev Physiol*,
825 *80*, 219-241. https://doi.org/10.1146/annurev-physiol-021317-121615
826 Gavello, D., Calorio, C., Franchino, C., Cesano, F., Carabelli, V., Carbone, E., & Marcantoni, A. (2018).
827 Early Alterations of Hippocampal Neuronal Firing Induced by Abeta42. *Cereb Cortex*, *28*(2),
828 433-446. https://doi.org/10.1093/cercor/bhw377
829 Gebhart, M., Juhasz-Vedres, G., Zuccotti, A., Brandt, N., Engel, J., Trockenbacher, A., Kaur, G.,
830 Obermair, G. J., Knipper, M., Koschak, A., & Striessnig, J. (2010). Modulation of Cav1.3 Ca2+
831 channel gating by Rab3 interacting molecule [Research Support, Non-U.S. Gov't]. *Mol Cell*
832 *Neurosci*, *44*(3), 246-259. https://doi.org/10.1016/j.mcn.2010.03.011
833 Genome BiolVandesompele, J., De Preter, K., Pattyn, F., Poppe, B., Van Roy, N., De Paepe, A., &
834 Speleman, F. (2002). Accurate normalization of real-time quantitative RT-PCR data by
835 geometric averaging of multiple internal control genes. *Genome biology*, *3*(7),
836 RESEARCH0034. https://doi.org/10.1186/gb-2002-3-7-research0034
837 Giguère, N., Burke Nanni, S., & Trudeau, L. E. (2018). On Cell Loss and Selective Vulnerability of
838 Neuronal Populations in Parkinson's Disease. *Front Neurol*, *9*, 455.
839 https://doi.org/10.3389/fneur.2018.00455
840 Grace, A. A., & Bunney, B. S. (1984a). The control of firing pattern in nigral dopamine neurons: burst
841 firing. *J Neurosci*, *4*(11), 2877-2890.
842 Grace, A. A., & Bunney, B. S. (1984b). The control of firing pattern in nigral dopamine neurons: single
843 spike firing. *J Neurosci*, *4*, 2866-2876.
844 Grundemann, J., Schlaudraff, F., & Liss, B. (2011). UV-laser microdissection and mRNA expression
845 analysis of individual neurons from postmortem Parkinson's disease brains. *Methods Mol*
846 *Biol*, *755*, 363-374. https://doi.org/10.1007/978-1-61779-163-5_30
847 Guarina, L., Calorio, C., Gavello, D., Moreva, E., Traina, P., Battiato, A., Ditalia Tchernij, S., Forneris, J.,
848 Gai, M., Picollo, F., Olivero, P., Genovese, M., Carbone, E., Marcantoni, A., & Carabelli, V.
849 (2018). Nanodiamonds-induced effects on neuronal firing of mouse hippocampal
850 microcircuits. *Sci Rep*, *8*(1), 2221. https://doi.org/10.1038/s41598-018-20528-5
851 Guzman, J. N., Ilijic, E., Yang, B., Sanchez-Padilla, J., Wokosin, D., Galtieri, D., Kondapalli, J.,
852 Schumacker, P. T., & Surmeier, D. J. (2018). Systemic isradipine treatment diminishes
853 calcium-dependent mitochondrial oxidant stress. *J Clin Invest*, *128*(6), 2266-2280.
854 https://doi.org/10.1172/JCI95898
855 Guzman, J. N., Sanchez-Padilla, J., Chan, C. S., & Surmeier, D. J. (2009). Robust pacemaking in
856 substantia nigra dopaminergic neurons. *J Neurosci*, *29*(35), 11011-11019.
857 https://doi.org/10.1523/JNEUROSCI.2519-09.2009 [doi]

858 Hess, M. E., Hess, S., Meyer, K. D., Verhagen, L. A., Koch, L., Bronneke, H. S., Dietrich, M. O., Jordan, S.
859 D., Saletore, Y., Elemento, O., Belgardt, B. F., Franz, T., Horvath, T. L., Ruther, U., Jaffrey, S. R.,
860 Kloppenburg, P., & Bruning, J. C. (2013). The fat mass and obesity associated gene (Fto)
861 regulates activity of the dopaminergic midbrain circuitry. *Nat Neurosci*, *16*(8), 1042-1048.
862 https://doi.org/10.1038/nn.3449
863 Hofer, N. T., Tuluc, P., Ortner, N. J., Nikonishyna, Y. V., Fernándes-Quintero, M. L., Liedl, K. R., Flucher,
864 B. E., Cox, H., & Striessnig, J. (2020). Biophysical classification of a CACNA1D de novo
865 mutation as a high-risk mutation for a severe neurodevelopmental disorder. *Molecular*
866 *autism*, *11*, 4. https://doi.org/10.1186/s13229-019-0310-4
867 Horn, R., & Marty, A. (1988). Muscarinic activation of ionic currents measured by a new whole-cell
868 recording method. *J Gen Physiol*, *92*(2), 145-159. https://doi.org/10.1085/jgp.92.2.145
869 Jones, L. P., Wei, S. K., & Yue, D. T. (1998). Mechanism of auxiliary subunit modulation of neuronal
870 alpha1E calcium channels. *J Gen Physiol*, *112*(2), 125-143.
871 http://www.ncbi.nlm.nih.gov/pubmed/9689023
872 Kepplinger, K. J., Forstner, G., Kahr, H., Leitner, K., Pammer, P., Groschner, K., Soldatov, N. M., &
873 Romanin, C. (2000). Molecular determinant for run-down of L-type Ca2+ channels localized in
874 the carboxyl terminus of the 1C subunit. *J Physiol*, *529 Pt 1*, 119-130.
875 https://doi.org/10.1111/j.1469-7793.2000.00119.x
876 Kim, J., Wei, D. S., & Hoffman, D. A. (2005). Kv4 potassium channel subunits control action potential
877 repolarization and frequency-dependent broadening in rat hippocampal CA1 pyramidal
878 neurones. *J Physiol*, *569*(Pt 1), 41-57. https://doi.org/10.1113/jphysiol.2005.095042
879 Kimm, T., & Bean, B. P. (2014). Inhibition of A-type potassium current by the peptide toxin SNX-482. *J*
880 *Neurosci*, *34*(28), 9182-9189. https://doi.org/10.1523/JNEUROSCI.0339-14.2014
881 Kiyonaka, S., Wakamori, M., Miki, T., Uriu, Y., Nonaka, M., Bito, H., Beedle, A. M., Mori, E., Hara, Y.,
882 De Waard, M., Kanagawa, M., Itakura, M., Takahashi, M., Campbell, K. P., & Mori, Y. (2007).
883 RIM1 confers sustained activity and neurotransmitter vesicle anchoring to presynaptic Ca2+
884 channels. *Nature neuroscience*, *10*(6). https://doi.org/10.1038/nn1904
885 Koschak, A., Reimer, D., Huber, I., Grabner, M., Glossmann, H., Engel, J., & Striessnig, J. (2001). alpha
886 1D (Cav1.3) subunits can form L-type Ca^{2+} channels activating at negative voltages. *J Biol*
887 *Chem*, *276*, 22100-22106. https://doi.org/10.1074/jbc.M101469200
888 Lacey, M. G., Mercuri, N. B., & North, R. A. (1989). Two cell types in rat substantia nigra zona
889 compacta distinguished by membrane properties and the actions of dopamine and opioids. *J*
890 *Neurosci*, *9*(4), 1233-1241. https://www.ncbi.nlm.nih.gov/pubmed/2703874

891 Lieb, A., Ortner, N., & Striessnig, J. (2014). C-terminal modulatory domain controls coupling of
892 voltage-sensing to pore opening in Cav1.3 L-type calcium channels. *Biophys J*, *106*(7), 1467-
893 1475. https://doi.org/10.1016/j.bpj.2014.02.017
894 Lindau, M., & Fernandez, J. M. (1986). IgE-mediated degranulation of mast cells does not require
895 opening of ion channels. *Nature*, *319*(6049), 150-153. https://doi.org/10.1038/319150a0
896 Link, S., Meissner, M., Held, B., Beck, A., Weissgerber, P., Freichel, M., & Flockerzi, V. (2009). Diversity
897 and developmental expression of L-type calcium channel beta2 proteins and their influence
898 on calcium current in murine heart. *J Biol Chem*, *284*(44), 30129-30137.
899 https://doi.org/10.1074/jbc.M109.045583
900 Liss, B. (2002). Improved quantitative real-time RT-PCR for expression profiling of individual cells.
901 *Nucleic Acids Res*, *30*(17), e89. https://doi.org/10.1093/nar/gnf088
902 Liss, B., Franz, O., Sewing, S., Bruns, R., Neuhoff, H., & Roeper, J. (2001). Tuning pacemaker frequency
903 of individual dopaminergic neurons by Kv4.3L and KChip3.1 transcription. *EMBO J*, *20*(20),
904 5715-5724. https://doi.org/10.1093/emboj/20.20.5715
905 Liss, B., & Striessnig, J. (2019). The Potential of L-Type Calcium Channels as a Drug Target for
906 Neuroprotective Therapy in Parkinson's Disease. *Annu Rev Pharmacol Toxicol*, *59*, 263-289.
907 https://doi.org/10.1146/annurev-pharmtox-010818-021214
908 Liu, H., De Waard, M., Scott, V. E. S., Gurnett, C. A., Lennon, V. A., & Campbell, K. P. (1996).
909 Identification of three subunits of the high affinity omega- Conotoxin MVIIC-sensitive calcium
910 channel. *J Biol Chem*, *271*, 13804-13810.
911 Matsushita, N., Okada, H., Yasoshima, Y., Takahashi, K., Kiuchi, K., & Kobayashi, K. (2002). Dynamics
912 of tyrosine hydroxylase promoter activity during midbrain dopaminergic neuron
913 development. *J Neurochem*, *82*(2), 295-304. https://doi.org/10.1046/j.1471-
914 4159.2002.00972.x
915 Matt, L., Kim, K., Chowdhury, D., & Hell, J. W. (2019). Role of Palmitoylation of Postsynaptic Proteins
916 in Promoting Synaptic Plasticity. *Front Mol Neurosci*, *12*, 8.
917 https://doi.org/10.3389/fnmol.2019.00008
918 Miranda-Laferte, E., Ewers, D., Guzman, R. E., Jordan, N., Schmidt, S., & Hidalgo, P. (2014). The N-
919 terminal domain tethers the voltage-gated calcium channel beta2e-subunit to the plasma
920 membrane via electrostatic and hydrophobic interactions. *J Biol Chem*, *289*(15), 10387-
921 10398. https://doi.org/10.1074/jbc.M113.507244
922 Miranda-Laferte, E., Schmidt, S., Jara, A. C., Neely, A., & Hidalgo, P. (2012). A short polybasic segment
923 between the two conserved domains of the beta2a-subunit modulates the rate of
924 inactivation of R-type calcium channel. *J Biol Chem*, *287*(39), 32588-32597.
925 https://doi.org/10.1074/jbc.M112.362509

926 Morgenstern, T. J., Park, J., Fan, Q. R., & Colecraft, H. M. (2019). A potent voltage-gated calcium
927 channel inhibitor engineered from a nanobody targeted to auxiliary CaVbeta subunits. *eLife*,
928 *8*. https://doi.org/10.7554/eLife.49253
929 Nakashima, Y. M., Todorovic, S. M., Pereverzev, A., Hescheler, J., Schneider, T., & Lingle, C. J. (1998).
930 Properties of Ba2+ currents arising from human alpha1E and alpha1Ebeta3 constructs
931 expressed in HEK293 cells: physiology, pharmacology, and comparison to native T-type Ba2+
932 currents. *Neuropharmacology*, *37*(8), 957-972. https://doi.org/10.1016/s0028-
933 3908(98)00097-5
934 Neher, E. (1992). Correction for liquid junction potentials in patch clamp experiments. *Methods*
935 *Enzymol*, *207*, 123-131. https://doi.org/10.1016/0076-6879(92)07008-c
936 Neuhoff, H., Neu, A., Liss, B., & Roeper, J. (2002). I(h) channels contribute to the different functional
937 properties of identified dopaminergic subpopulations in the midbrain. *J Neurosci*, *22*(4),
938 1290-1302.
939 Newcomb, R., Szoke, B., Palma, A., Wang, G., Chen, X., Hopkins, W., Cong, R., Miller, J., Urge, L.,
940 Tarczy-Hornoch, K., Loo, J. A., Dooley, D. J., Nadasdi, L., Tsien, R. W., Lemos, J., & Miljanich, G.
941 (1998). Selective peptide antagonist of the class E calcium channel from the venom of the
942 tarantula Hysterocrates gigas. *Biochemistry*, *37*(44), 15353-15362.
943 Ortner, N. J., Bock, G., Dougalis, A., Kharitonova, M., Duda, J., Hess, S., Tuluc, P., Pomberger, T.,
944 Stefanova, N., Pitterl, F., Ciossek, T., Oberacher, H., Draheim, H. J., Kloppenburg, P., Liss, B., &
945 Striessnig, J. (2017). Lower Affinity of Isradipine for L-Type Ca(2+) Channels during Substantia
946 Nigra Dopamine Neuron-Like Activity: Implications for Neuroprotection in Parkinson's
947 Disease. *J Neurosci*, *37*(28), 6761-6777. https://doi.org/10.1523/JNEUROSCI.2946-16.2017
948 Ortner, N. J., Bock, G., Vandael, D. H., Mauersberger, R., Draheim, H. J., Gust, R., Carbone, E., Tuluc,
949 P., & Striessnig, J. (2014). Pyrimidine-2,4,6-triones are a new class of voltage-gated L-type
950 Ca^{2+} channel activators. *Nat Commun*, *5*, 3897. https://doi.org/10.1038/ncomms4897
951 Ortner, N. J., Pinggera, A., Hofer, N. T., Siller, A., Brandt, N., Raffeiner, A., Vilusic, K., Lang, I., Blum, K.,
952 Obermair, G. J., Stefan, E., Engel, J., & Striessnig, J. (2020). RBP2 stabilizes slow Cav1.3 Ca2+
953 channel inactivation properties of cochlear inner hair cells. *Pflügers Archiv: European Journal*
954 *of Physiology*, *472*(1), 3-25. https://doi.org/10.1007/s00424-019-02338-4
955 Ortner, N. J., Pinggera, A., Hofer, N. T., Siller, A., Brandt, N., Raffeiner, A., Vilusic, K., Lang, I., Blum, K.,
956 Obermair, G. J., Stefan, E., Engel, J., & Striessnig, J. (2020). RBP2 stabilizes slow Cav1.3 Ca(2+)
957 channel inactivation properties of cochlear inner hair cells. *Pflugers Arch*, *472*(1), 3-25.
958 https://doi.org/10.1007/s00424-019-02338-4
959 Paladini, C. A., & Roeper, J. (2014). Generating bursts (and pauses) in the dopamine midbrain
960 neurons. *Neuroscience*, *282*, 109-121. https://doi.org/10.1016/j.neuroscience.2014.07.032

961 Parkinson Study Group, S.-P. D. I. I. I. I. (2020). Isradipine Versus Placebo in Early Parkinson Disease: A
962 Randomized Trial. *Ann Intern Med*, *172*(9), 591-598. https://doi.org/10.7326/M19-2534
963 Paxinos, G., & Franklin, K. B. J. (2004). *The Mouse Brain in Stereotaxic Coordinates*.
964 Pereverzev, A., Leroy, J., Krieger, A., Malecot, C. O., Hescheler, J., Pfitzer, G., Klockner, U., &
965 Schneider, T. (2002). Alternate splicing in the cytosolic II-III loop and the carboxy terminus of
966 human E-type voltage-gated Ca(2+) channels: electrophysiological characterization of
967 isoforms. *Mol Cell Neurosci*, *21*(2), 352-365. https://doi.org/10.1006/mcne.2002.1179
968 Philippart, F., Destreel, G., Merino-Sepúlveda, P., Henny, P., Engel, D., & Seutin, V. (2016). Differential
969 Somatic Ca2+ Channel Profile in Midbrain Dopaminergic Neurons. *J Neurosci*, *36*, 7234-7245.
970 https://doi.org/10.1523/JNEUROSCI.0459-16.2016
971 Pruszak, J., Just, L., Isacson, O., & Nikkhah, G. (2009). Isolation and culture of ventral mesencephalic
972 precursor cells and dopaminergic neurons from rodent brains. *Curr Protoc Stem Cell Biol*,
973 *Chapter 2*, Unit 2D.5. https://doi.org/10.1002/9780470151808.sc02d05s11
974 Puopolo, M., Raviola, E., & Bean, B. P. (2007). Roles of subthreshold calcium current and sodium
975 current in spontaneous firing of mouse midbrain dopamine neurons. *J Neurosci*, *27*(3), 645-
976 656. https://doi.org/10.1523/JNEUROSCI.4341-06.2007
977 Qin, N., Platano, D., Olcese, R., Costantin, J. L., Stefani, E., & Birnbaumer, L. (1998). Unique regulatory
978 properties of the type 2a Ca2+ channel beta subunit caused by palmitoylation. *Proceedings*
979 *of the National Academy of Sciences of the United States of America*, *95*(8), 4690-4695.
980 Rae, J., Cooper, K., Gates, P., & Watsky, M. (1991). Low access resistance perforated patch recordings
981 using amphotericin B. *J Neurosci Methods*, *37*(1), 15-26. https://doi.org/10.1016/0165-
982 0270(91)90017-t
983 Randall, A. D., & Tsien, R. W. (1997). Contrasting biophysical and pharmacological properties of T-
984 type and R-type calcium channels. *Neuropharmacology*, *36*(7), 879-893.
985 https://doi.org/10.1016/s0028-3908(97)00086-5
986 Richards, C. D., Shiroyama, T., & Kitai, S. T. (1997). Electrophysiological and immunocytochemical
987 characterization of GABA and dopamine neurons in the substantia nigra of the rat.
988 *Neuroscience*, *80*(2), 545-557. https://doi.org/10.1016/s0306-4522(97)00093-6
989 Robinson, B. G., Cai, X., Wang, J., Bunzow, J. R., Williams, J. T., & Kaeser, P. S. (2019). RIM is essential
990 for stimulated but not spontaneous somatodendritic dopamine release in the midbrain.
991 *eLife*, *8*, e47972. https://doi.org/10.7554/eLife.47972
992 Sawamoto, K., Nakao, N., Kobayashi, K., Matsushita, N., Takahashi, H., Kakishita, K., Yamamoto, A.,
993 Yoshizaki, T., Terashima, T., Murakami, F., Itakura, T., & Okano, H. (2001). Visualization, direct
994 isolation, and transplantation of midbrain dopaminergic neurons. *Proc Natl Acad Sci U S A*,
995 *98*(11), 6423-6428. https://doi.org/10.1073/pnas.111152398

Schiemann, J., Schlaudraff, F., Klose, V., Bingmer, M., Seino, S., Magill, P. J., Zaghloul, K. A., Schneider, G., Liss, B., & Roeper, J. (2012). K-ATP channels in dopamine substantia nigra neurons control bursting and novelty-induced exploration. *Nat Neurosci*, *15*(9), 1272-1280. https://doi.org/10.1038/nn.3185

Schlick, B., Flucher, B. E., & Obermair, G. J. (2010). Voltage-activated calcium channel expression profiles in mouse brain and cultured hippocampal neurons. *Neuroscience*, *167*(3), 786-798. https://doi.org/10.1016/j.neuroscience.2010.02.037

Schneider, T., Alpdogan, S., Hescheler, J., & Neumaier, F. (2018). In vitro and in vivo phosphorylation of the Cav2.3 voltage-gated R-type calcium channel. *Channels (Austin)*, *12*(1), 326-334. https://doi.org/10.1080/19336950.2018.1516984

Schneider, T., Dibue, M., & Hescheler, J. (2013). How "Pharmacoresistant" is Cav2.3, the Major Component of Voltage-Gated R-type Ca2+ Channels? *Pharmaceuticals (Basel)*, *6*(6), 759-776. https://doi.org/10.3390/ph6060759

Scott, V. E., De Waard, M., Liu, H., Gurnett, C. A., Venzke, D. P., Lennon, V. A., & Campbell, K. P. (1996). Beta subunit heterogeneity in N-type Ca2+ channels. *J Biol Chem*, *271*(6), 3207-3212.

Shin, W. (2015). *RNASeq of DA neurons from SNpc and VTA. Dataset posted on 04.03.2015, 16:01 by William Shin*. https://figshare.com/articles/RNASeq_of_DA_neurons_from_SNpc_and_VTA/926519

Simons, C., Benkert, J., Deuter, N., Poetschke, C., Pongs, O., Schneider, T., Duda, J., & Liss, B. (2019). NCS-1 Deficiency Affects mRNA Levels of Genes Involved in Regulation of ATP Synthesis and Mitochondrial Stress in Highly Vulnerable Substantia nigra Dopaminergic Neurons. *Front Mol Neurosci*, *12*, 252. https://doi.org/10.3389/fnmol.2019.00252

Sochivko, D., Pereverzev, A., Smyth, N., Gissel, C., Schneider, T., & Beck, H. (2002). The Ca(V)2.3 Ca(2+) channel subunit contributes to R-type Ca(2+) currents in murine hippocampal and neocortical neurones. *J Physiol*, *542*(Pt 3), 699-710.

Soong, T. W., Stea, A., Hodson, C. D., Dubel, S. J., Vincent, S. R., & Snutch, T. P. (1993). Structure and functional expression of a member of the low voltage-activated calcium channel family. *Science*, *260*, 1133-1136.

Subramaniam, M., Althof, D., Gispert, S., Schwenk, J., Auburger, G., Kulik, A., Fakler, B., & Roeper, J. (2014). Mutant α-synuclein enhances firing frequencies in dopamine substantia nigra neurons by oxidative impairment of A-type potassium channels. *The Journal of Neuroscience: The Official Journal of the Society for Neuroscience*, *34*, 13586-13599. https://doi.org/10.1523/JNEUROSCI.5069-13.2014

1029 Surmeier, D. J., Guzman, J. N., Sanchez-Padilla, J., & Goldberg, J. A. (2011). The origins of oxidant
1030 stress in Parkinson's disease and therapeutic strategies. *Antioxid Redox Signal*, *14*(7), 1289-
1031 1301. https://doi.org/10.1089/ars.2010.3521
1032 Surmeier, D. J., Obeso, J. A., & Halliday, G. M. (2017). Selective neuronal vulnerability in Parkinson
1033 disease. *Nat Rev Neurosci*, *18*, 101-113. https://doi.org/10.1038/nrn.2016.178
1034 Tomagra, G., Picollo, F., Battiato, A., Picconi, B., De Marchis, S., Pasquarelli, A., Olivero, P.,
1035 Marcantoni, A., Calabresi, P., Carbone, E., & Carabelli, V. (2019). Quantal Release of
1036 Dopamine and Action Potential Firing Detected in Midbrain Neurons by Multifunctional
1037 Diamond-Based Microarrays. *Front Neurosci*, *13*, 288.
1038 https://doi.org/10.3389/fnins.2019.00288
1039 Tottene, A., Moretti, A., & Pietrobon, D. (1996). Functional diversity of P-type and R-type calcium
1040 channels in rat cerebellar neurons. *J Neurosci*, *16*(20), 6353-6363. 8815914
1041 Wang, G., Dayanithi, G., Newcomb, R., & Lemos, J. R. (1999). An R-type Ca(2+) current in
1042 neurohypophysial terminals preferentially regulates oxytocin secretion. *J Neurosci*, *19*(21),
1043 9235-9241.
1044 Weiergraber, M., Henry, M., Sudkamp, M., de Vivie, E. R., Hescheler, J., & Schneider, T. (2005).
1045 Ablation of Ca(v)2.3 / E-type voltage-gated calcium channel results in cardiac arrhythmia and
1046 altered autonomic control within the murine cardiovascular system. *Basic Res Cardiol*,
1047 *100*(1), 1-13. https://doi.org/10.1007/s00395-004-0488-1
1048 Williams, M. E., Marubio, L. M., Deal, C. R., Hans, M., Brust, P. F., Philipson, L. H., Miller, R. J.,
1049 Johnson, E. C., Harpold, M. M., & Ellis, S. B. (1994). Structure and functional characterization
1050 of neuronal alpha1E calcium channel subtypes. *J Biol Chem*, *269*, 22347-22357.
1051 Xu, W., & Lipscombe, D. (2001). Neuronal $Ca_v1.3\alpha1$ L-type channels activate at relatively
1052 hyperpolarized membrane potentials and are incompletely inhibited by dihydropyridines. *J*
1053 *Neurosci*, *21*(16), 5944-5951. 11487617
1054 Yasuda, T., Chen, L., Barr, W., McRory, J. E., Lewis, R. J., Adams, D. J., & Zamponi, G. W. (2004).
1055 Auxiliary subunit regulation of high-voltage activated calcium channels expressed in
1056 mammalian cells. *Eur J Neurosci*, *20*(1), 1-13. 15245474
1057 Ye, J. H., Zhang, J., Xiao, C., & Kong, J. Q. (2006). Patch-clamp studies in the CNS illustrate a simple
1058 new method for obtaining viable neurons in rat brain slices: glycerol replacement of NaCl
1059 protects CNS neurons. *J Neurosci Methods*, *158*(2), 251-259.
1060 https://doi.org/10.1016/j.jneumeth.2006.06.006

1061

1062 **Figures and Tables**

1063

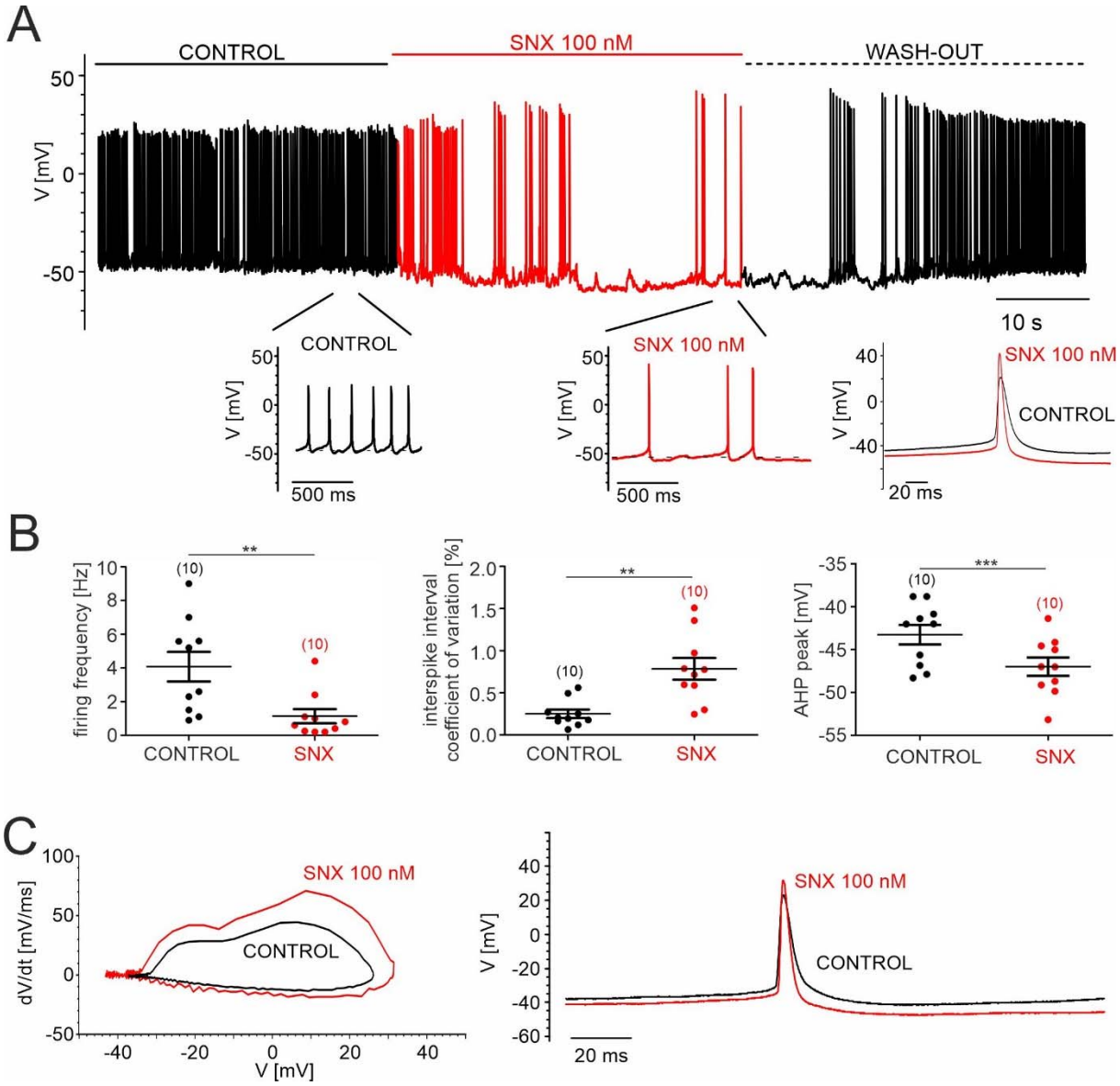

1064

1065 **Figure 1. SNX-482 effects on pacemaking of cultured mouse midbrain DA neurons.**
1066 **A.** Representative recording of spontaneous firing activity of cultured midbrain dopaminergic
1067 neurons before, during and after the application (wash-out) of 100 nM SNX-482. Inset (bottom
1068 right): overlay of one single AP before (control) and during the application of 100 nM SNX-482.
1069 **B.** Firing frequency [Hz], coefficient of variation of the interspike interval [%], and AHP peak
1070 [mV] before (control) and during the application of 100 nM SNX-482. Data represent the means
1071 ± SEM for the indicated number of experiments (N=3). Statistical significance was determined
1072 using paired Student's t-test.: *** $p<0.001$; ** $p<0.01$; * $p<0.05$. **C.** Left panel: Phase-plane plot
1073 analysis (time derivative of voltage (dV/dt) vs. voltage (V)) before (control) and during the
1074 application of 100 nM SNX-482. Right panel: corresponding AP trace in control and in the
1075 presence of SNX-482.

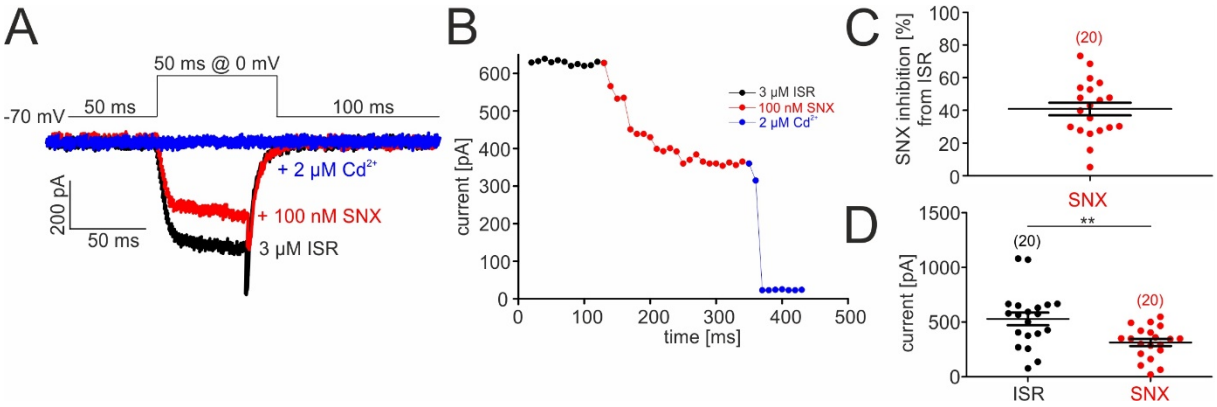

Figure 2. SNX-482 inhibition of non-L-type I_{Ca} in cultured midbrain DA neurons.

A. Representative traces illustrating the inhibition of non-L-type I_{Ca} by 100 nM SNX-482 (red). Cells were initially perfused with a bath solution containing 3 μM isradipine (ISR, black). Full block was obtained using 2 μM Cd^{2+} (blue). Square pulses (50 ms) were applied to 0 mV from a holding potential of -70 mV (top) **B.** Current amplitude values plotted as a function of time. After stabilization of I_{Ca} with ISR (black circles), 100 nM SNX-482 was applied. The remaining currents was blocked by 2 μM Cd^{2+}. **C.** SNX-482 inhibition expressed as % of control I_{Ca} after LTCC block using 3 μM ISR. **D.** Mean current amplitude at the end of ISR application and at the end of SNX-482 application. Data represent the means ± SEM for the indicated number of experiments (N=4). Statistical significance was determined using paired Student's t-test: *** $p<0.001$; ** $p<0.01$; * $p<0.05$.

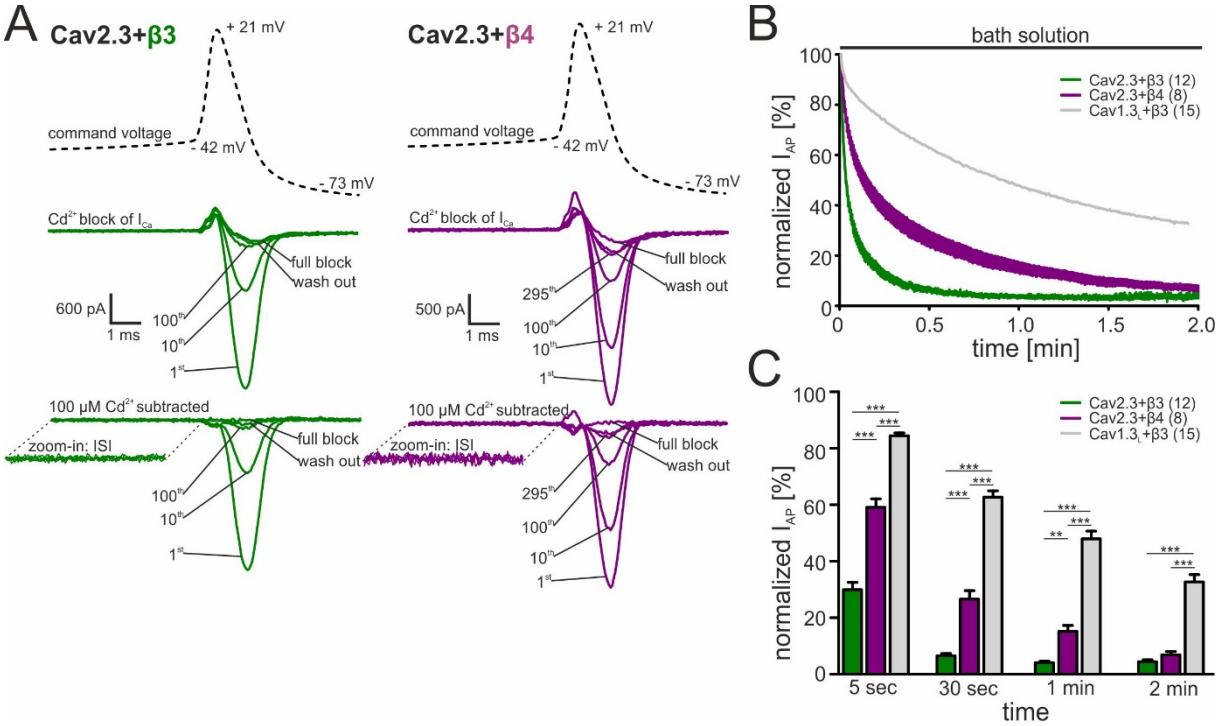

Figure 3. Activity-dependent inactivation of Cav2.3 channels co-transfected with β3 or β4 (and α2δ1) during simulated SN DA neuron regular pacemaking activity in tsA-201 cells.

A. Top panel: The SN DA neuron-derived command voltage was applied with a frequency of 2.5 Hz (only a time interval around the AP-spike is shown). Middle panel: Corresponding representative Ca^{2+} current traces (2 mM charge carrier) for Cav2.3 channels co-expressed with α2δ1 and β3 (green) or β4 (purple). Cav2.3 currents were completely blocked by 100 µM Cadmium (Cd^{2+}), and remaining Cd^{2+}-insensitive current components were subtracted off-line (bottom panel). ISI, interspike interval. **B.** Current decay during simulated 2.5 Hz SN DA neuron pacemaking. Normalized peak inward current during APs (I_{AP}) is plotted against time as mean ± SEM for the indicated number of experiments. I_{AP} amplitudes were normalized to the I_{AP} amplitude of the first AP after holding the cell at -89 mV. $Cav1.3_L$ co-expressed with α2δ1 and β3 (gray, mean only) is shown for comparison (data taken from Ortner et al., 2017). The I_{AP} decay was fitted to a bi-exponential function (Cav2.3 β3: A_{slow} = 39.4 ± 0.65 %, τ_{slow} = 22.2 ± 0.15 min, A_{fast} = 54.2 ± 0.76 %, τ_{fast} = 2.86 ± 0.07 min, non-inactivating = 4.47 ± 0.13 %; β4: A_{slow} = 48.5 ± 0.26 %, τ_{slow}= 90.3 ± 1.07 min, A_{fast} = 41.8 ± 0.40 %, τ_{fast} = 8.39 ± 0.16 min, non-inactivating = 5.12 ± 0.12 %). Curves represent the means ± SEM for the indicated number of experiments (N = Cav2.3/β3: 4; Cav2.3/β4: 2; $Cav1.3_L$/β3: 6). **C.** Normalized I_{AP} decay after predefined time points for Cav2.3 with β3 or β4 and $Cav1.3_L$ (with β3). Statistical significance was determined using one-way ANOVA followed by Bonferroni post-hoc test: *** $p<0.001$; ** $p<0.01$; * $p<0.05$.

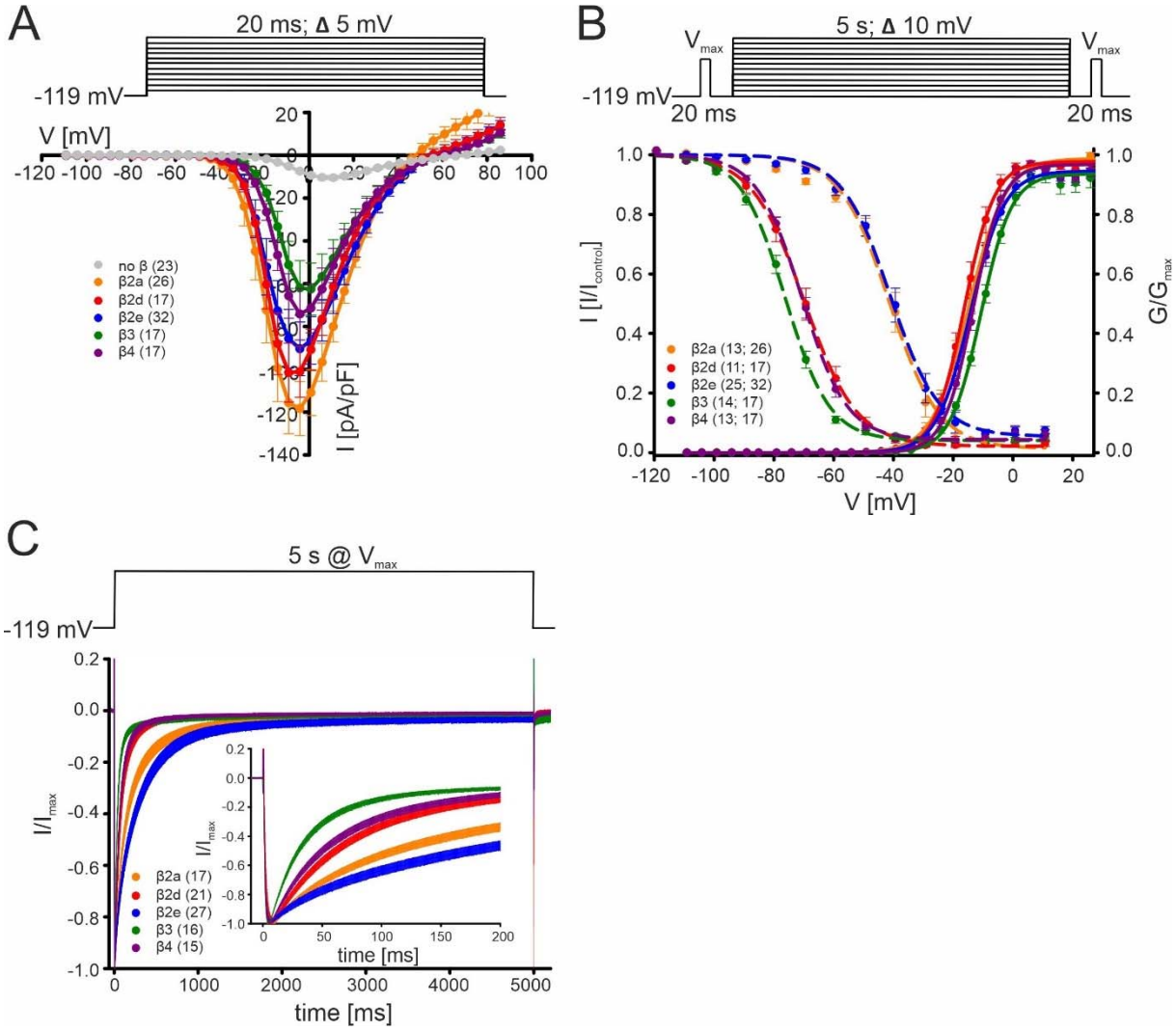

Figure 4. Biophysical properties of Cav2.3 channels co-transfected with different β-subunits (and α2δ1) in tsA-201 cells.

A. Current densities (pA/pF) with or without (gray) co-transfection of indicated β-subunits. Color code and n-numbers are given in the graphs. **B.** Voltage-dependence of steady-state activation (normalized conductance G, right axis, solid lines) and inactivation (normalized I_{Ca} of test pulses, left axis, dashed lines, left n-numbers in parentheses). **C.** Inactivation time course during 5 s depolarizing pulses to V_{max} starting from a holding potential of -119 mV. Inset shows the first 200 ms of the 5 s pulse. Respective stimulation protocols are shown above each graph. The curves represent the means ± SEM for the indicated number of experiments (N = β2a: 5; β2d, β2e: 2; β3, β4, no β: 3). For statistics see Table 1. V_{max}, voltage of maximal inward current.

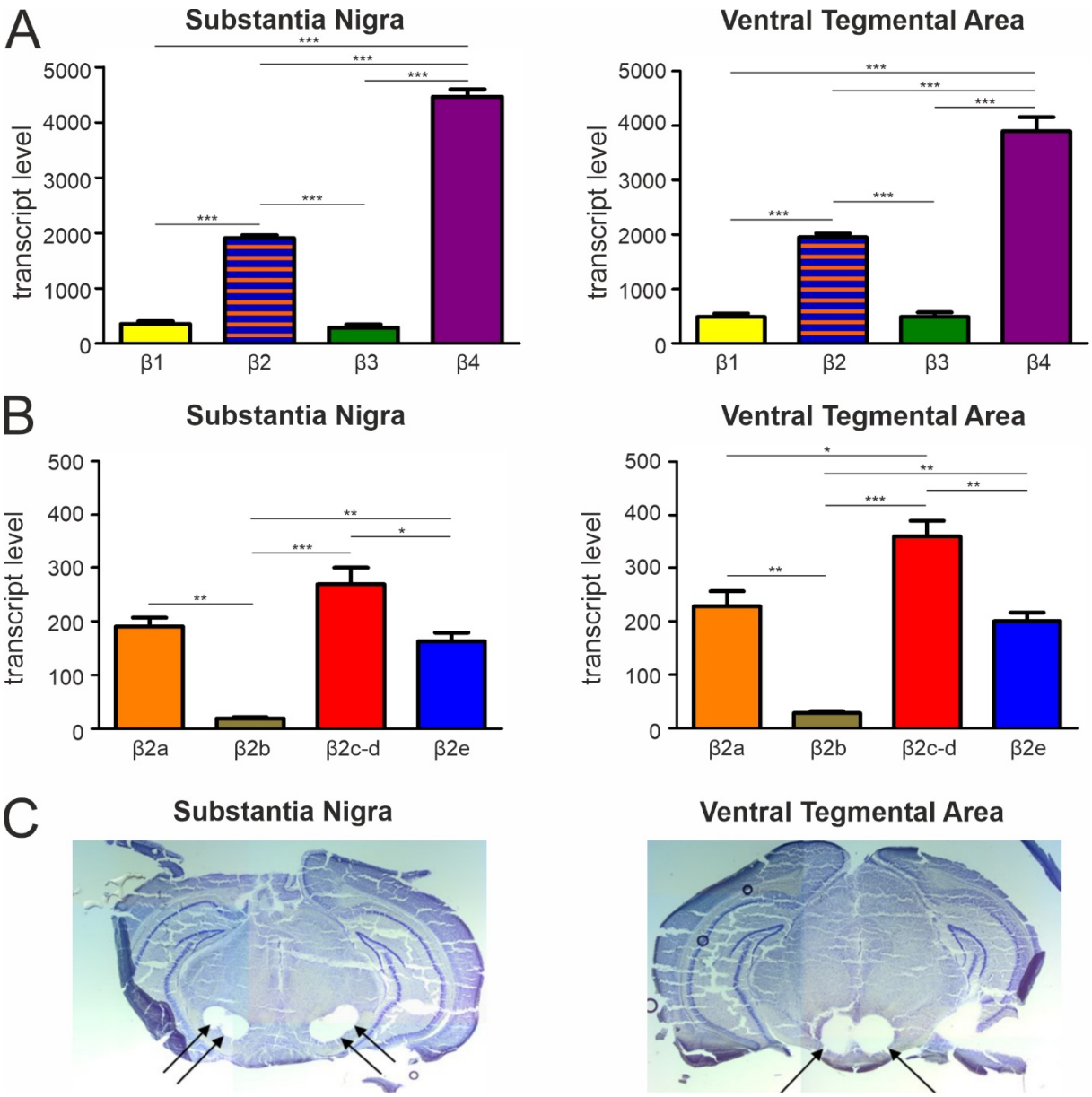

Figure 5. Transcript expression of various β-subunits and β2-subunit splice variants in mouse SN and VTA tissue.

A. Expression of β1-β4 subunit transcripts in SN (n=3, N=3) (left) and VTA (n=3, N=3) (right) determined by RT-qPCR as described in Methods. **B.** Expression of β2a-β2e subunit transcripts in SN (n=3, N=3) (left) and VTA (n=3, N=3) (right). Data are shown as the mean ± SEM. Statistical significance was determined using one-way ANOVA followed by Bonferroni post-hoc test: *** $p<0.001$; ** $p<0.01$; * $p<0.05$. Data was normalized to *Gapdh* and *Tfrc* determined by geNorm.

C. Example for four SN (left) and two VTA (right) tissue punches obtained for cDNA preparation with diameters of 0.5 mm each (left) or 0.8 mm each (right) from 7-8 successive 100-µm-sections between Bregma -3.00 mm and -3.80 mm, stained with Cresyl violet.

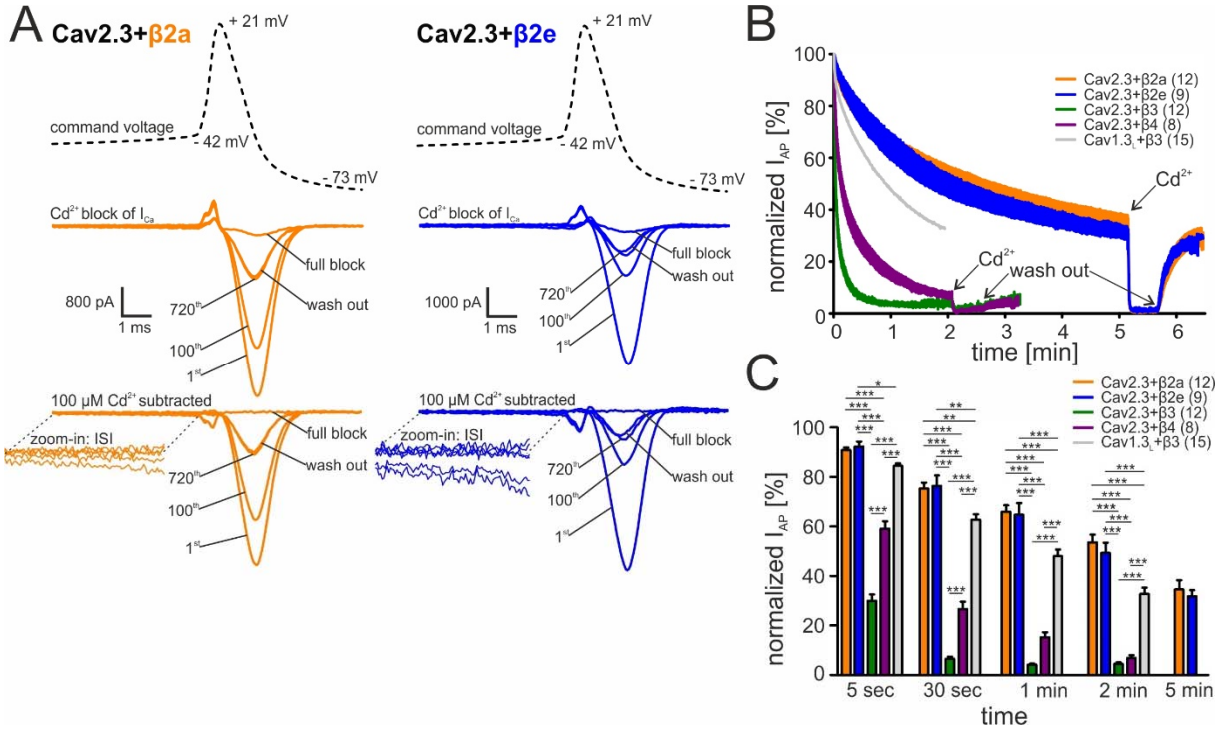

Figure 6. Activity-dependent inactivation of Cav2.3 channels co-transfected with β2a or β2e (and α2δ1) during simulated SN DA neuron regular pacemaking activity in tsA-201 cells.

A. Top panel: The SN DA neuron-derived command voltage was applied with a frequency of 2.5 Hz (only a time interval around the AP-spike is shown). Middle panel: Corresponding representative Ca^{2+} current traces (2 mM charge carrier) for Cav2.3 channels co-expressed with α2δ1 and β2a (orange) or β2e (blue). Cav2.3 currents were completely blocked by 100 µM Cadmium (Cd^{2+}) and remaining Cd^{2+}-insensitive current components were subtracted off-line (bottom panel). **B.** Current decay (normalized I_{AP}) is plotted over time as described in Fig. 3. Cav2.3 β3 (green), β4 (purple) and Cav1.3$_L$/β3 data are shown for comparison (see Fig. 3). The curves represent the means ± SEM for the indicated number of experiments (N = β2a: 4; β2e: 2; β3: 4; β4: 2; Cav1.3$_L$/β3: 6). The I_{AP} decay was fitted using a bi-exponential function (Cav2.3 β2a: A_{slow} = 52.6 ± 0.47 %, τ_{slow} = 299.3 ± 10.2 min, A_{fast} = 13.4 ± 0.53 %, τ_{fast} = 18.2 ± 1.47 min, non-inactivating = 32.3 ± 0.77 %; β2e: A_{slow} = 67.7 ± 0.11 %, τ_{slow} = 294.1 ± 1.77 min, A_{fast} = 7.10.0 ± 0.27 %, τ_{fast} = 16.6 ± 1.24 min, non-inactivating = 25.0 ± 0.12%). **C.** Normalized I_{AP} decay after predefined time points for Cav2.3 with co-expressed β2a, β2e, β3 or β4 and Cav1.3$_L$ (with β3). Statistical significance was determined using one-way ANOVA followed by Bonferroni post-hoc test (5s, 30s, 1 min, 2 min) or unpaired Student's t-test (5 min): *** p<0.001; ** p<0.01; * p<0.05.

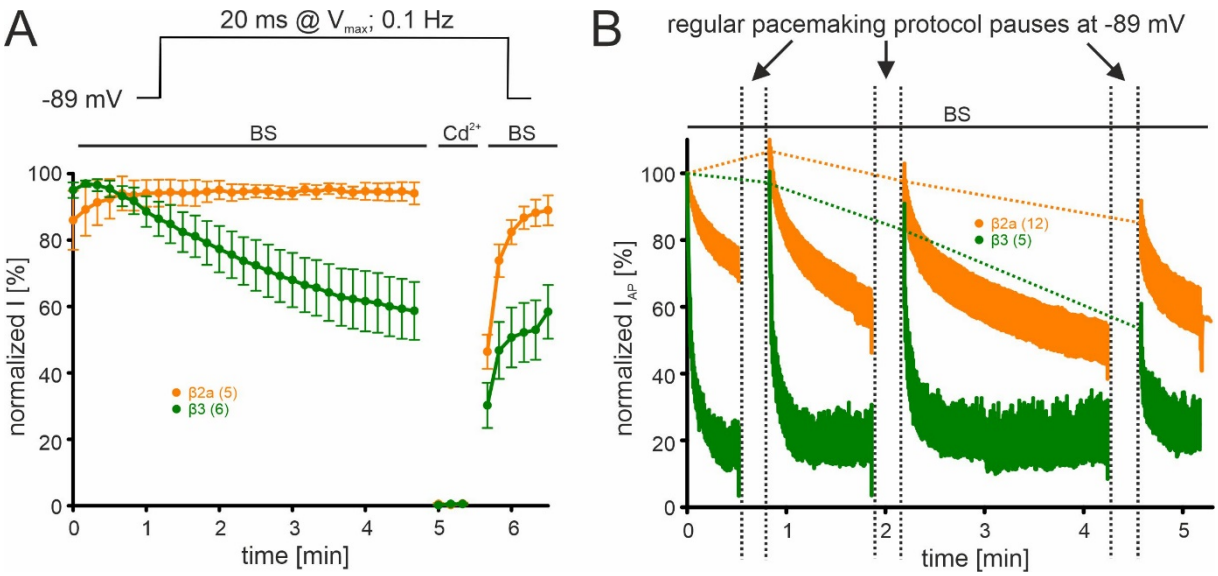

Figure 7. β-subunit-dependent run-down of Cav2.3 channel Ca^{2+} current in tsA-201 cells. Data for Cav2.3 co-expressed with α2δ1 and β2a (orange) or β3 (green) are shown**. A.** Run-down during a 0.1 Hz square pulse protocol (20 ms to V_{max}, hp -89 mV). Currents were normalized to the I_{Ca} of the sweep with the maximal peak inward current observed during the recording. After a full block with 100 µM Cd^{2+} currents recovered to the amplitude preceding the Cd^{2+} application. **B.** Cells were held at -89 mV and then stimulated using the regular SN DA neuron pacemaking protocol for 30 s, 1 min, and 2 min each followed by 20 s long pauses (vertical dashed lines) at hyperpolarized potentials (-89 mV) to allow channel recovery from inactivation. I_{AP} of individual APs was normalized to the inward current of the first AP. The current run-down component can be estimated from the non-recovering current component (horizontal dashed lines). Traces represent means ± SEM from the indicated number of experiments (N=2). BS, bath solution

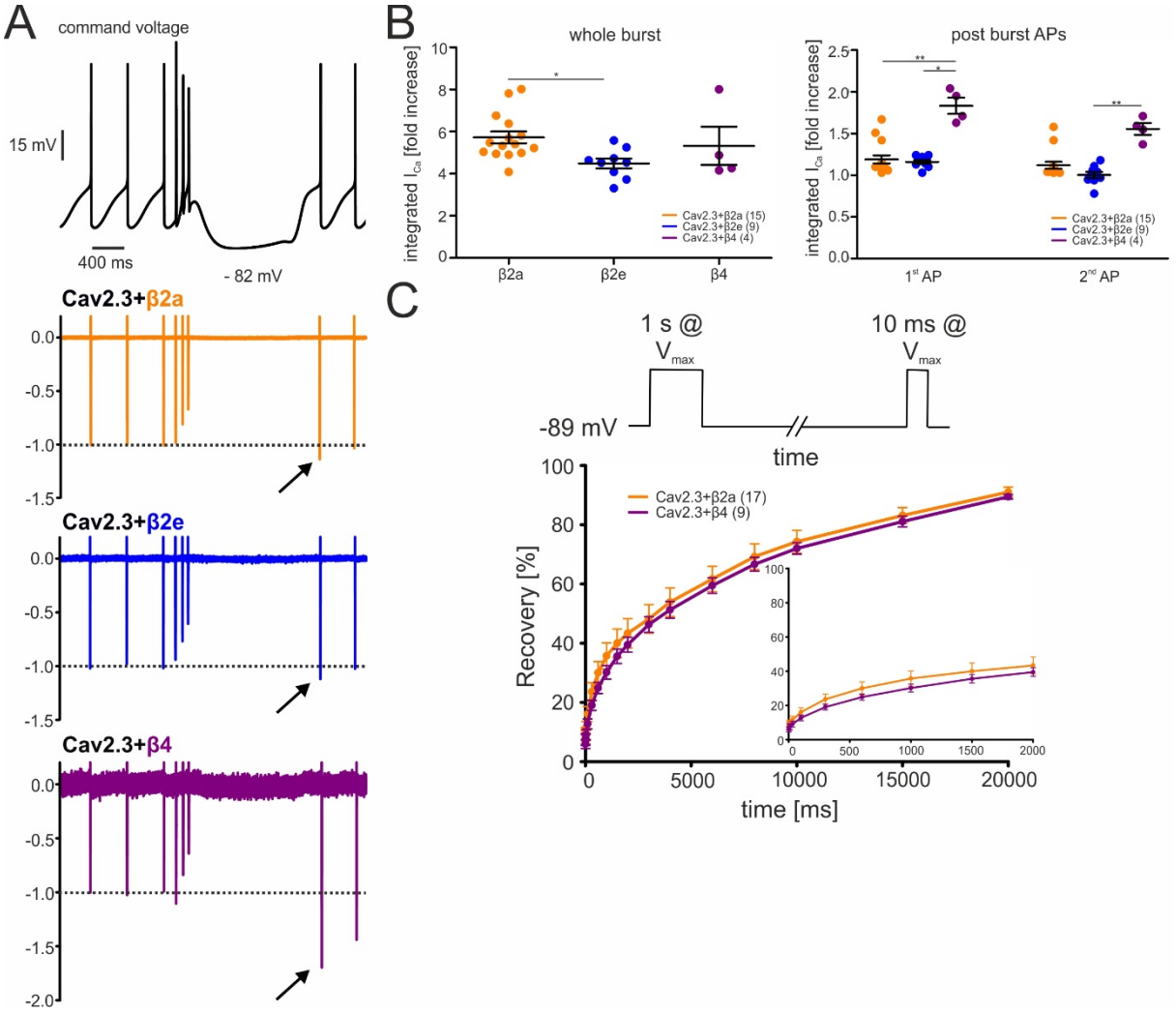

Figure 8. Effects of different β-subunits on Cav2.3 currents during a simulated SN DA neuron three-spike burst and post-burst APs in tsA-201 cells.

The burst command voltage was elicited after ~5-6 min (β2a, β2e) or ~1-2 min (β4) of regular pacemaking to reach steady-state I_{AP} (β2a and β2e: ~30% of the initial I_{AP}, β4: ~6% of the initial I_{AP}, see Fig. 6). **A.** Normalized current responses of Cav2.3 channels co-expressed with β2a, β2e or β4 subunits (and α2δ1) induced by a command voltage (top panel) simulating a typical three-spike burst followed by a hyperpolarization phase at hyperpolarized potentials (lowest voltage: -82 mV) for 1.5 seconds. Remaining Cd^{2+}-insensitive current components (100 µM Cd^{2+}) were subtracted off-line to extract pure Cav2.3 mediated I_{Ca}. One of at least four experiments with similar results is shown. **B.** The integrated I_{Ca} during a single AP before the burst (obtained as the mean of the three preceding APs) was set to 100 % and compared with I_{Ca} during the three-spike burst integrated over the time period equivalent to one AP (left) or the first APs after the pause (right). All investigated β-subunits resulted in increased integrated I_{Ca} during the burst. Data represent the means ± SEM for the indicated number of experiments (N = β2a: 4; β2e: 2; β4: 2). Statistical significance was determined using one-way ANOVA followed by Bonferroni post-test (whole burst) or Kruskal-Wallis followed by Dunn's multiple comparison test (post-burst APs): *** p<0.001; ** p<0.01; * p<0.05. **C.** Square-pulse protocol

1188 (top) used to determine recovery from inactivation after the indicated time intervals for β2a and
1189 β4-associated Cav2.3 channels (see Methods for details). Data represent the means ± SEM
1190 for the indicated number of experiments (N=3). For statistics see Table 2.

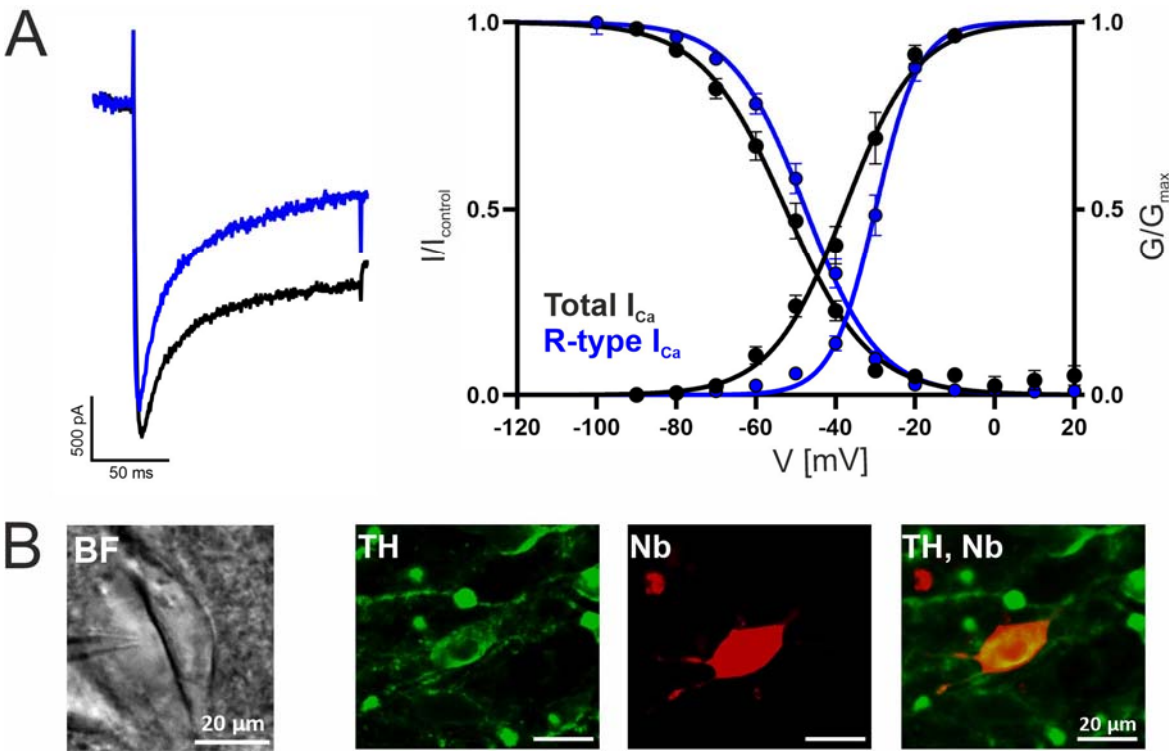

Figure 9. Voltage-dependence of gating of R-type currents in mouse SN DA neurons. I_{Ca} recorded in SN DA neurons without (black traces/symbols) or after preincubation (blue) of slices with a Cav channel blocker cocktail to inhibit Cav3 (10 µM Z941), Cav1 (1 µM isradipine), Cav2.1 and Cav2.2 (1 µM ω-conotoxin-MVIIC). **A.** Left panel: representative current traces of recordings of steady-state activation (at -20 mV test potential, similar amplitudes were chosen). Right panel: voltage-dependence of steady-state activation and inactivation, curve fits to the mean values (± SEM) are shown. **B.** Exemplary neuron as seen under the patch clamp microscope with patch pipette next to it (left; BF, brightfield) and a neuron after histochemical staining for tyrosine hydroxylase (TH, green) and neurobiotin (Nb, red). Detailed parameters and statistics are given in Table 3.

Tables

	Cav2.3 - Activation 2 mM Ca^{2+}						Cav2.3 - Inactivation 2 mM Ca^{2+}			
β-subunit	**$V_{0.5}$ [mV]**	**k [mV]**	**V_{rev} [mV]**	**act thresh [mV]**	**current density [pA/pF]**	**n**	**$V_{0.5, inact}$ [mV]**	**k_{inact} [mV]**	**plateau [%]**	**n**
no β					-10.7 ±1.1	23				
β2a	-14.8 ±1.2	4.8 ±0.2	37.1 ±0.9	-32.0 ±0.9	-130.0^{+++} ±15.2	26	-40.6 ±1.8	7.3 ±0.6	1.67 ±1.26	13
$^{C3S/C4S}$β2a	-13.9 ±1.7	4.7 ±0.3	38.2 ±1.1	-30.9 ±0.7	-105.7^{+++} ±21.4	12	-62.6$^{***/\#\#\#/\S\S\S}$ ±1.6	8.3$^{\#\#}$ ±0.4	4.57 ±1.63	9
β2d	-15.9§ ±1.1	4.6 ±0.2	37.2 ±1.1	-32.1§ ±0.7	-107.7^{+++} ±13.4	17	-69.6$^{***/\#\#\#}$ ±1.8	8.2$^{\#\#}$ ±0.1	2.09 ±0.72	11
β2e	-14.1 ±0.9	4.8 ±0.2	40.3* ±0.6	-31.5 ±0.7	-96.8^{+++} ±14.3	32	-39.6 ±2.4	6.5 ±0.3	4.06 ±1.63	25
β3	-10.5 ±0.7	5.2 ±0.2	39.8 ±0.9	-29.2 ±0.7	-64.6^{++} ±12.8	17	-76.2$^{***/\#\#\#}$ ±1.0	7.0 ±0.1	4.12 ±0.70	14
β4	-13.1 ±0.7	5.0 ±0.2	38.5 ±0.5	-31.0 ±0.5	-74.8^{+++} ±11.9	17	-70.4$^{***/\#\#\#}$ ±1.2	7.3 ±0.2	4.06 ±1.80	13

Cav2.3 - 5 s Inactivation time course 2 mM Ca^{2+}							
β-subunit	**r50 [%]**	**r100 [%]**	**r250 [%]**	**r500 [%]**	**r1000 [%]**	**r5000 [%]**	**n**
β2a	71.3 ±2.1	52.4 ±2.8	27.8 ±2.9	14.3 ±2.3	6.5 ±1.2	1.3 ±0.3	17
$^{C3S/C4S}$β2a	67.4$^{\S\S\S/\%}$ ±5.2	47.3$^{\#/\S\S\S/\%\%}$ ±6.4	23.4§ ±5.3	11.6 ±3.3	6.2 ±1.7	3.4 ±1.1	11
β2d	57.4$^{*/\#\#\#/\S\S\S}$ ±2.8	32.6$^{***/\#\#\#/\S\S}$ ±2.4	11.3$^{*/\#\#\#}$ ±1.7	4.4$^{**/\#\#\#}$ ±0.9	2.4$^{**/\#\#\#}$ ±0.6	1.7 ±0.5	21
β2e	77.5 ±2.9	64.2 ±3.3	41.1 ±3.2	22.3 ±2.8	10.1 ±2.0	3.3 ±0.8	27
β3	32.9$^{***/\#\#\#}$ ±2.9	14.2$^{***/\#\#\#}$ ±1.5	6.1$^{***/\#\#\#}$ ±1.0	4.4$^{**/\#\#\#}$ ±0.7	2.9$^{\#}$ ±0.5	1.6 ±0.3	16
β4	50.3$^{***/\#\#\#/\S\S}$ ±2.7	27.1$^{***/\#\#\#}$ ±2.5	8.6$^{**/\#\#\#}$ ±1.4	3.7$^{**/\#\#\#}$ ±0.8	2.0$^{**/\#\#\#}$ ±0.5	1.0 ±0.2	15

Table 1. Voltage-dependence of activation and inactivation, and time course of inactivation of Cav2.3 co-transfected with α2δ1 and different β subunits in tsA-201 cells.

All values are given as means ± SEM for the indicated number of experiments (N = β2a: 5; $^{C3S/C4S}$β2a, β2d, β2e: 2; β3, β4, no β: 3). Voltage-dependence of gating: $V_{0.5}$, Half-maximal activation voltage; k, slope factor; V_{rev}, estimated reversal potential; act thresh, activation threshold; $V_{0.5,inact}$, half-maximal inactivation voltage; k_{inact}, inactivation slope factor; plateau, remaining non-inactivating current. Near physiological recording conditions (2 mM Ca^{2+}, low 0.5 mM EGTA Ca^{2+} buffering) and calculation of the parameters of voltage-dependence of activation and inactivation are described in Materials and Methods. Statistical significance was determined using one-way ANOVA with Bonferroni post-hoc test ($V_{0.5}$, V_{rev}, $V_{0.5,inact}$, k_{inact}, plateau) or Kruskal-Wallis followed by Dunn's multiple comparison test (k, act thresh, current

density). Statistical significances of post-hoc tests are indicated for comparison vs. β2a (*, **, ***), vs. β2e ($^{\#}$, $^{\#\#}$, $^{\#\#\#}$), vs. β3 (§, §§, §§§) and vs. no β ($^{+}$, $^{++}$, $^{+++}$): $p<0.05$, $p<0.01$, $p<0.001$. Inactivation time course: The r values represent the fraction of I_{Ca} remaining after 50, 100, 250, 500, 1000 or 5000 ms during a 5 s pulse to V_{max} (voltage of maximal inward current). Statistical significance was determined using one-way ANOVA with Bonferroni post-hoc test (r100) or Kruskal-Wallis followed by Dunn's multiple comparison test (r50, r250, r500, r1000, r5000). Statistical significances of post hoc tests are indicated for comparison vs. β2a (*, **, ***), vs. β2e ($^{\#}$, $^{\#\#}$, $^{\#\#\#}$), vs. β3 (§, §§, §§§) or vs β4 ($^{\%}$, $^{\%\%}$, $^{\%\%\%}$): $p<0.05$, $p<0.01$, $p<0.001$.

Cav2.3 - recovery from inactivation 2 mM Ca^{2+}					
β-subunit	**r100 [%]**	**r1500 [%]**	**r4000 [%]**	**r10000 [%]**	**n**
β2a	15.7 ±2.4	39.3 ±4.6	53.4 ±4.5	74.2 ±3.6	17
β4	12.7 ±1.7	35.6 ±2.4	51.3 ±2.8	72.0 ±1.9	9

1225
1226 **Table 2. Recovery from inactivation of Cav2.3 channels co-transfected with either β2a**
1227 **or β4 in combination with α2δ1 in tsA-201 cells.**
1228 All values are presented as the mean ± SEM for the indicated number of experiments (N=3).
1229 The r values represent the fraction of recovered I_{Ca} after 100, 1500, 4000 or 10000 ms at -89
1230 mV between depolarizations to V_{max}. No statistical significance was observed (unpaired
1231 Student's t-test).
1232

	Activation			Inactivation		
	$V_{0.5,act}$ [mV]	k_{act} [mV]	n/N	$V_{0.5, inact}$ [mV]	k_{inact} [mV]	n/N
Control	-37.4±1.8	7.2±0.58	16/8	-52.4±1.58	9.57±0.54	16/8
+ T-, L-, N-, P/Q-Cav blockers	-29.7±1.07**	4.42±0.28***	19/5	-47.5±1.38*	8.15±0.37	19/5
+ 100 nM SNX-482	-42.7±2.3	7.73±0.65	8/2	-51.3±1.35	10.7±0.85	9/2

1233
1234 **Table 3. Voltage-dependence of activation and inactivation of Ca^{2+}-currents in SN DA**
1235 **neurons**
1236 Whole cell patch-clamp experiments were performed as described in Methods in cells
1237 preincubated with a cocktail blocking T-, L-, N-, and P/Q-Ca^{2+} channels (10μM Z941, 1μM
1238 isradipine, 1μM ω-conotoxin-MVIIC) to isolate R-type currents. N, number of preparations; n,
1239 number of experiments. Voltages were not corrected for liquid junction potential (- 5mV).
1240 Statistics: ****, $p<0.0001$; *, $p<0.05$ (vs. control, Mann–Whitney U test).
1241
1242

1243 **Supplement**

1244 **Supplemental Figures**

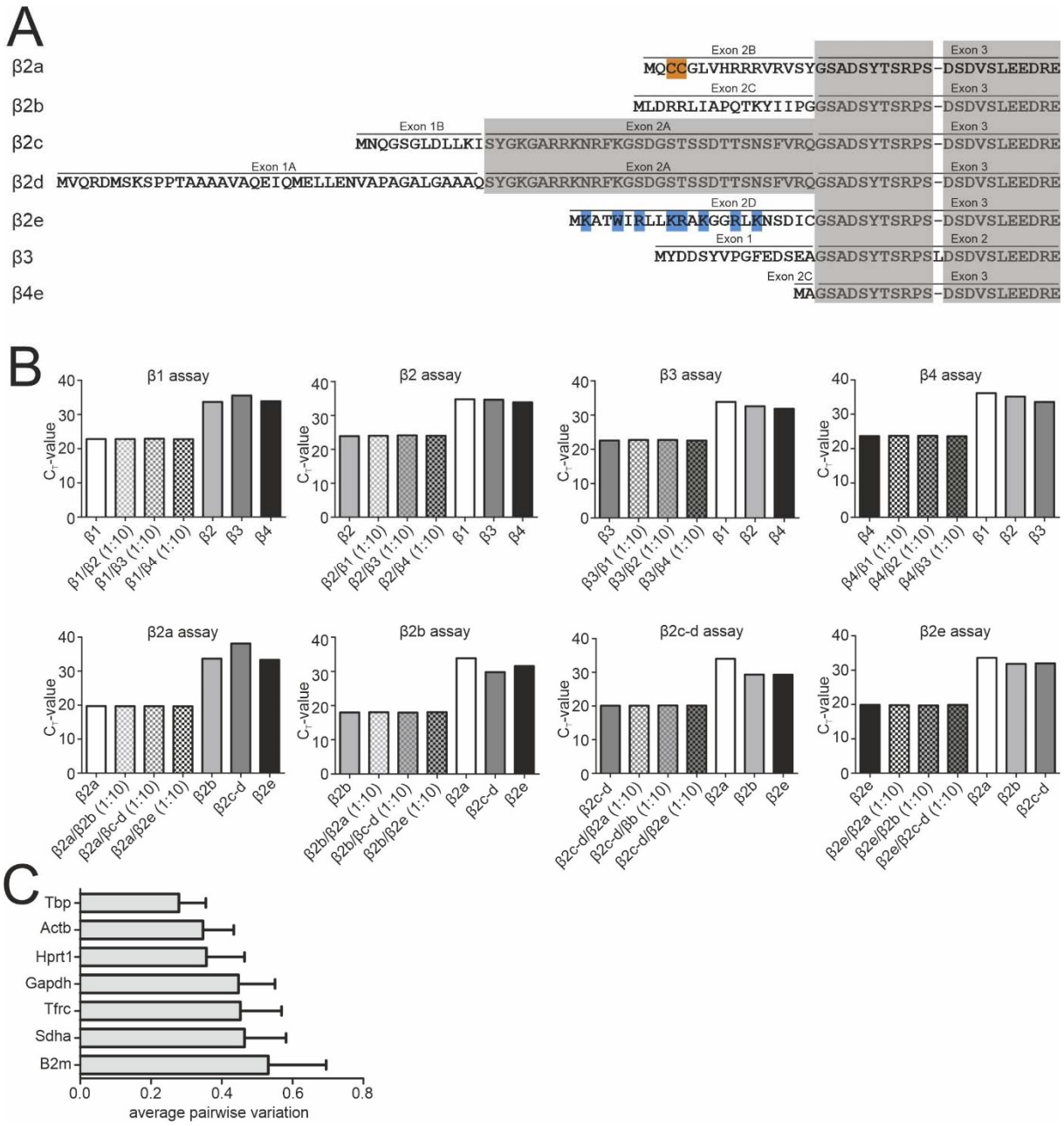

1245

1246 **Supplemental Figure 1. Binding specificity of β1-β4 and β2a-β2e TaqMan assays and**
1247 **expression stability of endogenous control genes.**

1248 **A.** Alignment of the N-terminal amino acid sequence of the investigated β-subunits (β2a, β2d,
1249 β2e, β3 or β4). Residues responsible for membrane anchoring of β2a (palmitoylated cysteine
1250 residues are highlighted in orange) and β2e (positively charged amino acids forming a lipid
1251 binding motif are highlighted in blue) are indicated. Homologous exons are shaded in grey.
1252 Sequence accession numbers (human): β2a (NP_000715.2), β2d (NP_963887.2), β2e
1253 (NP_963864.1), β3 (NP_000716.2), β4e (NP_001307651.1). **B.** The indicated β-subunit
1254 isoforms (β1-β4; n=6) and β2 splice variants (n=3) were recognized with high specificity (low

1255 CT value) by the corresponding RT-qPCR assay even in the presence of a 10-fold higher
1256 concentration of the mismatching DNA fragments corresponding to other isoforms/splice
1257 variants (β1-4: n=2; β2 splice variants: n=1). High binding specificity was confirmed by
1258 inefficient detection (high CT value) of all non-matching DNA fragments. **C.** Average
1259 expression stability of endogenous control genes in SN and VTA tissue. All reference genes
1260 maintained comparable cDNA concentrations throughout the experiments. Data were
1261 normalized to the expression of *Gapdh* and *Tfrc* determined by geNorm. Data are given as
1262 means ± SEM (n=6, N=6).
1263

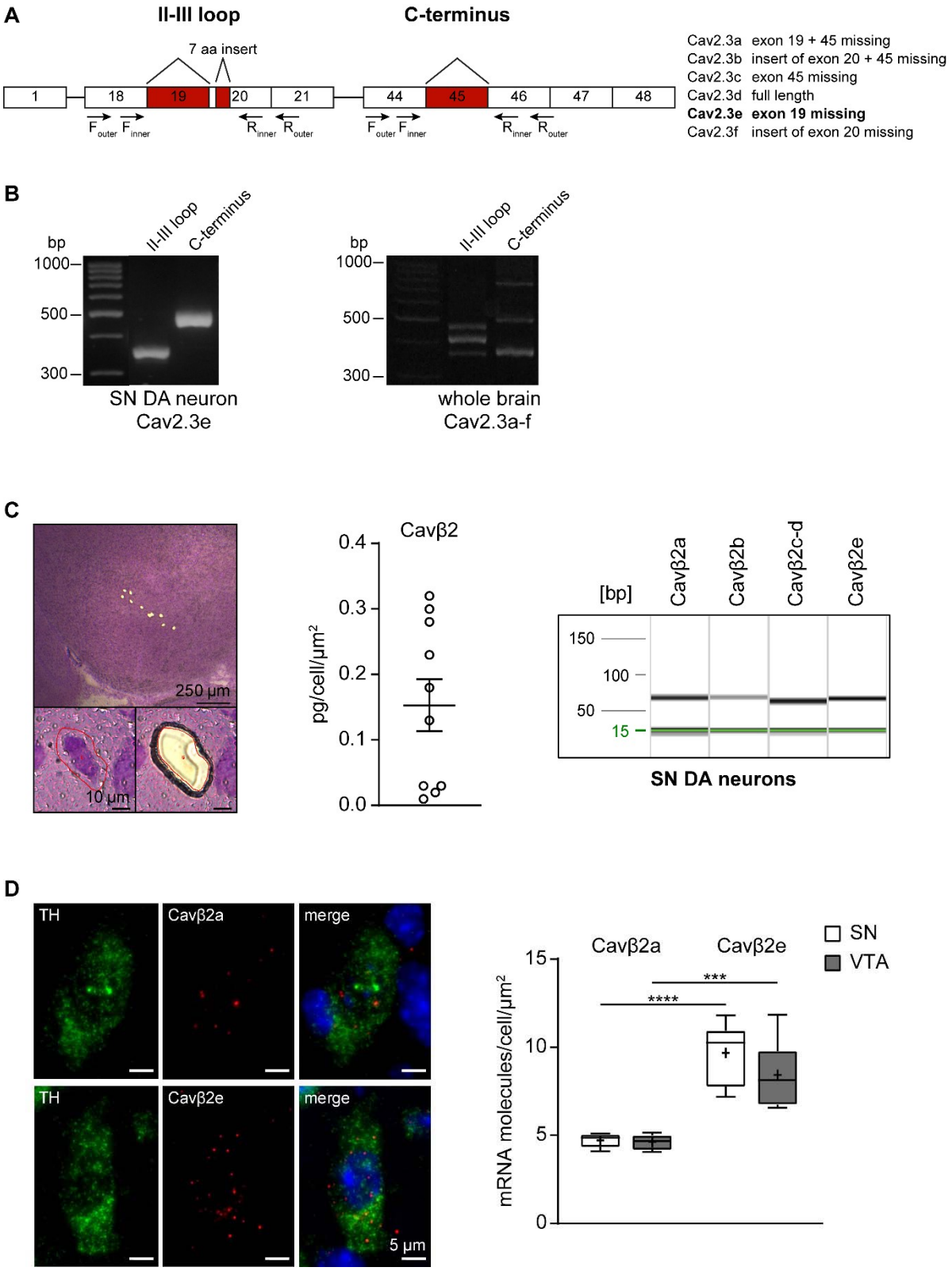

Supplemental Figure 2. Determination of the expressed Cav2.3 splice variants in SN DA neurons.

A. Cartoon of the exon structure of all Cav2.3 splice variants. The murine Cacna1e gene, coding for the Cav2.3 α1-subunits contains 48 exons with six major alternative splice variants (right panel). The splicing events include the variable use of exon 19, 21 nucleotides of exon

1271 20 and exon 45. The outer and inner primer pairs chosen for identification of the different splice
1272 variants are located in the II-III loop and the C-terminus, covering the three described splicing
1273 sites. Expressed exons are shown as white boxes and splicing sites are indicated in red. **B**.
1274 Agarose gel electrophoresis image showing two PCR products (363 bp II-III loop nested PCR
1275 fragment and 498 bp C-terminus nested PCR fragment) coding for the Cav2.3e splice variant
1276 found in mouse laser-dissected SN DA neuron derived cDNA (n=40, left). In contrast, all five
1277 PCR products (363 bp, 399 bp and 420 bp in the II-III loop and 369 bp and 498 bp in the C-
1278 terminus nested PCR fragments) coding for all six major splice variants were found in whole
1279 brain tissue-derived cDNA (as positive control, right panel).
1280 **C.** Left: Overview of a cresyl violet (CV) stained coronal midbrain section of a juvenile wildtype
1281 mouse after UV-LMD of 10 SN DA neurons (scale bar: 250 µm, upper). Image of one CV
1282 stained SN DA neuron of a juvenile wildtype mouse before and after UV-LMD (scale bar: 10
1283 µm, lower). Middle: β2-subunit transcript relative mRNA quantification by reverse transcription
1284 quantitative PCR-based in UV-LMD mouse SN DA neurons (n = 10). Right: Capillary gel
1285 electrophoresis image illustrating PCR products of β2-subunit splice variants amplified from a
1286 UV-LMD cDNA template corresponding to 2.9 cells. **D.** Left: Representative images showing
1287 β2a and β2e (red) or tyrosine hydroxylase (TH, green) RNAScope fluorescence signals
1288 (combined with nuclear DAPI staining, blue) of individual SN DA neurons from an adult wildtype
1289 mouse. Scale bar: 5 µm. Right: Absolute mRNA transcript numbers per cell for β2a or β2e in
1290 adult SN DA and VTA DA neurons of adult wildtype mice (N = 6, each), as indicated. Tukey's
1291 boxplots are shown. Significances are indicated by asterisks: *** $p < 0.001$, **** $p < 0.0001$.
1292 For statistics see details in Suppl. Table 4.

1293

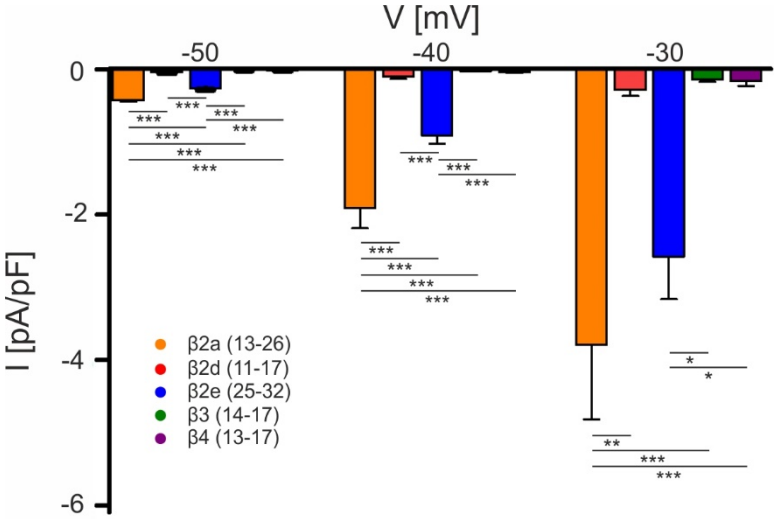

Supplemental Figure 3. Window currents of Cav2.3 co-expressed with α2δ1 and different β-subunits.

Window currents measured in the presence of the indicated β-subunits were calculated by multiplying mean current densities (pA/pF) of I-V-relationships by the fractional current inactivation from steady-state inactivation curves at the indicated voltages. Color code and n-numbers are shown in the graph. Data represent the means ± SEM for the indicated number of experiments (N = β2a: 5; β2d, β2e: 2; β3, β4: 3). Statistical significance was determined using one-way ANOVA with Bonferroni post-hoc test and is indicated: *** $p<0.001$; ** $p<0.01$; * $p<0.05$.

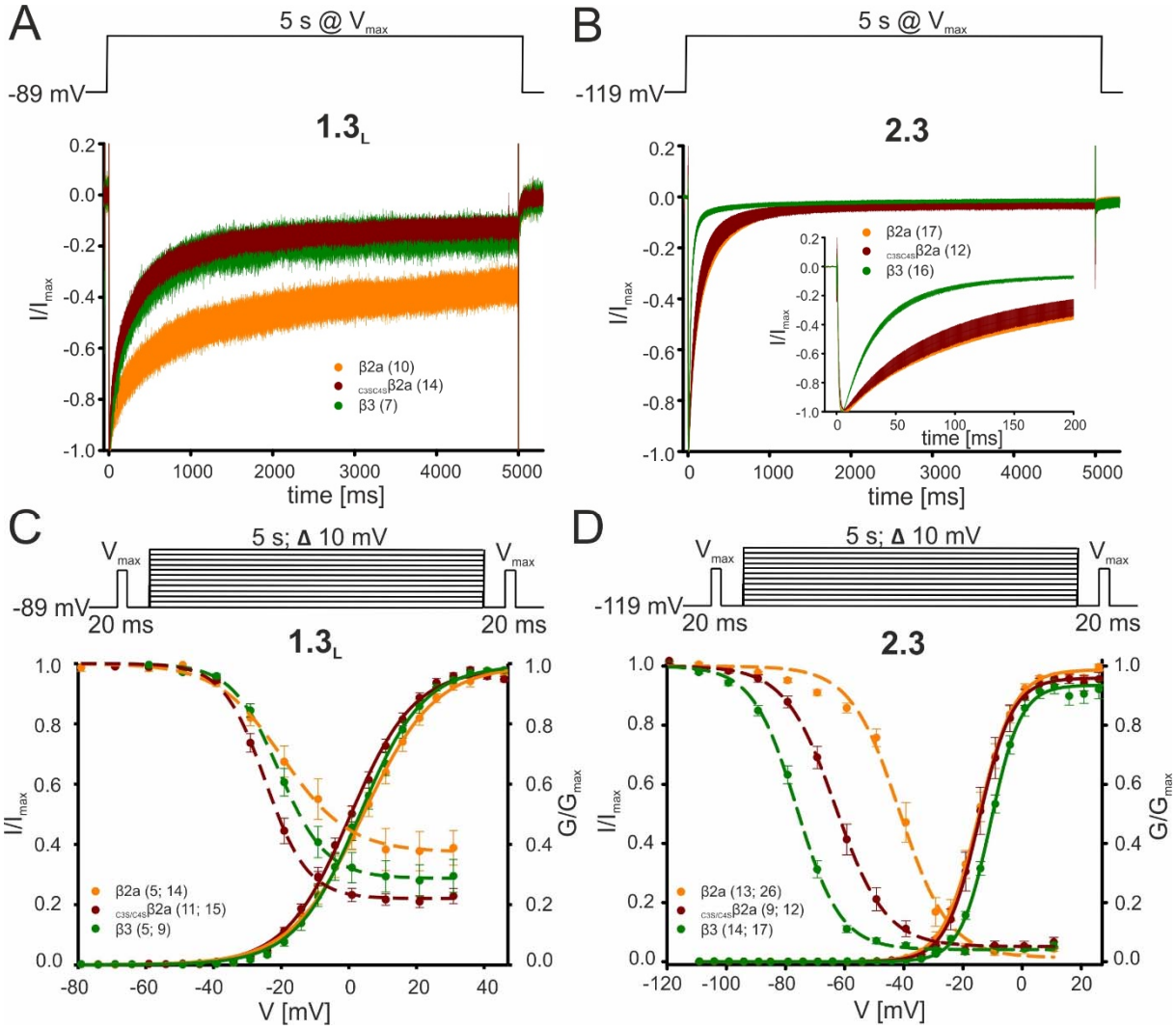

Suppl. Figure 4. Effect of β2a palmitoylation on the biophysical properties of Cav2.3 and Cav1.3 Ca^{2+} channels in tsA-201 cells.

Data are shown for Cav1.3 (C-terminally long splice variant, Bock et al., 2011) or Cav2.3 α1-subunits co-expressed with α2δ1 and β2a (orange), C3S/C4Sβ2a (red) or β3 (green). Respective command voltages are given in each panel. To disrupt palmitoylation-mediated membrane anchoring, the two N-terminal cysteines of β2a (see Suppl Fig. 1A) were replaced by serines in C3S/C4Sβ2a. **A, B.** Inactivation kinetics during a 5 s long depolarizing step to V_{max} for Cav1.3$_L$ (**A**, 15 mM Ca^{2+}, hp -89 mV) or Cav2.3 (**B**, 2 mM Ca^{2+}, hp -119 mV). Curves represent means ± SEM for the indicated number of experiments. For statistics see Tables 1 and Suppl. Table 6. **C, D.** Voltage-dependence of activation (solid lines, normalized conductance G) and inactivation (dashed lines, normalized I_{Ca} of 20 ms test pulses) for Cav1.3$_L$ (**C,** 15 mM Ca^{2+}, hp -89 mV) or Cav2.3 (**D**, 2 mM Ca^{2+}, hp -119 mV). Means ± SEM. For statistics see Tables 1 and Suppl. Table 6.

Unlike β2a, C3S/C4Sβ2a was unable to slow the inactivation time course of L-type channels, such as Cav1.3, thus stabilizing faster inactivation similar to β3 (Suppl. Table 6, Gebhart et al., 2010). In contrast, preventing palmitoylation of β2a did not affect the inactivation time course

of Cav2.3e (Table 1). Moreover, unlike observed for Cav2.3, steady-state inactivation was not significantly different for Cav1.3 co-transfected with β2a, β3, or $_{C3S/C4S}$β2a (Suppl. Table 6). In contrast, compared to β4 and β3, $_{C3S/C4S}$β2a significantly shifted $V_{0.5,inact}$ of Cav2.3 to more positive voltages but to a much smaller extent than β2a (+35 mV) (Table 1).

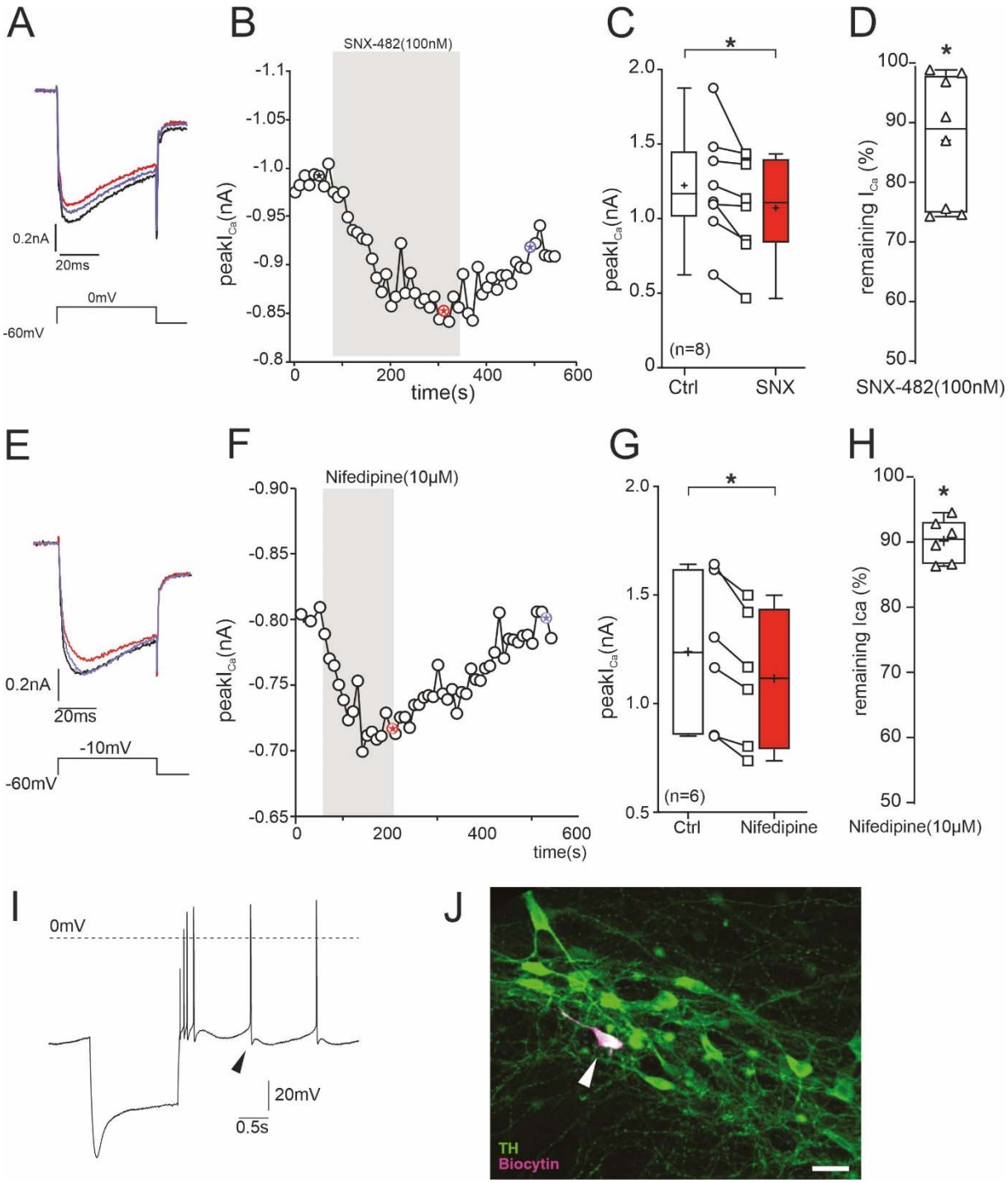

Suppl. Figure 5: **Inhibition of I_{Ca} in SN DA neurons of adult (12 weeks) mice by 100 nM SNX-482.**

To further prove the presence of SNX-482-sensitive R-type currents in SN DA neurons we performed perforated-patch recordings. These allow stable recordings over a long period of time and to test for reversibility of channel block by 100 nM SNX-482. Recordings were performed with the pulse protocol shown in A (holding potential -60 mV) after blocking I_A K^+-currents known to be present in these cells to exclude block of I_A by SNX-482 (Kimm & Bean, 2014) as described previously (Benkert et al., 2019). 100 nM SNX-482 significantly reduced

current to 87 ± 4% of control I_{Ca} (n=8, p=0.012, one-sample t-test, for statistics see Suppl. Table 6) and this inhibition was slowly reversible. **A.** I_{Ca} before (black), during (red) and after (blue) SNX-482 application. **B.** Example of peak I_{Ca} plotted over time during SNX-482 application. The asterisks mark the time points of the recordings shown on the left. Single depolarizing voltage steps to 0 mV were applied from a holding potential of -60 mV every 10 s. **C.** Mean effect of SNX-482 on peak I_{Ca}. *, p<0.05 (n=8; two-tailed paired t-test). **D.** Remaining peak I_{Ca} after SNX-482 inhibition. *, p<0.05 (two-tailed one sample t-test). Box plots: Whiskers indicate minimal and maximal values, '+'-sign: mean, horizontal line: median. No complete concentration-response curves were generated since higher concentrations of SNX-482 are known to also inhibit other Cav channels (Bourinet et al., 2001; Newcomb et al., 1998). Therefore, our experiments may underestimate the overall contribution of Cav2.3 channel to total I_{Ca}, also because a fraction of channels must already be inactivated at the selected holding potential (-60 mV) of these experiments.

E. - H. Under identical experimental conditions, nifedipine reduced I_{Ca} to 90 ± 1.4% of control (p=0.031, Wilcoxon-test, for statistics see Suppl. Table 6), and this inhibition was fully reversible. **E.** Perforated patch-clamp recording of I_{Ca} before (black), during (red) and after (blue) nifedipine application. **F.** Example of peak I_{Ca} plotted over time during nifedipine application. The asterisks mark the time points of the recordings shown on the left. Single depolarizing voltage steps to -10 mV were applied from a holding potential of -60 mV every 10 s. **G.** Mean effect of nifedipine on peak I_{Ca}. *, p<0.05 (n=6; two-tailed paired t-test). **H.** Remaining peak I_{Ca} under nifedipine. p<0.05 (two-tailed Wilcoxon signed-rank test). Box plots: Whiskers indicate minimal and maximal values, '+'-sign: mean, horizontal line: median. For statistics see Suppl. table 6.

I. Current clamp recording of a DA neuron in the SN pars compacta to demonstrate the pre-identifying electrophysiological properties including sag potential during hyperpolarization, broad action potentials, and regular pacemaking. Arrowhead: largely reduced slow afterhyperpolarization due to partial block of K^+ channels by Cs^+ diffusion into the neuron during the perforation process. **J.** Post recording analysis shows co-localization of biocytin (recorded neuron; magenta) and tyrosine hydroxylase (TH, green).

1368 **Supplemental Tables**

β-subunit	genbank accession no.	assay ID or sequences for custom assay	exon boundary	primer sequences for standard template cloning	fragment length (bp)
β1	NM_031173.4	Mm00518940_m1	2/3	Fwd: 5´-ATATGTCGACTCTCCATGGTCCAGAAGAGC-3´ Rev: 5´-CTTGAAGCTTGTACTTCTCCTTGATGTGTA-3´	455
β2	NM_023116.4	Mm01333550_m1	13/14	Fwd: 5´-ATATGTCGACAATGTCAGATACAGCGCAGC-3 Rev: 5'-CTTGAAGCTTTGTTACACTGTTTGCACTGG-3'	419
β3	NM_007581.3	Mm00432233_m1	1/2	Fwd: 5´-ATATGTCGACCCCATGTATGACGACTCCTACG-3 Rev: 5'-CTTGAAGCTTACAGTAGCTGACATTGGTCCTCAC-3'	236
β4	NM_146123.3	Mm00521623_m1	11/12	Fwd: 5´-ATATGTCGACGCTGATTAAGTCCAGAGGAAAGTC-3 Rev: 5'-CTTGAAGCTTTGTCTCATTCGCTGACTCTGTAAT-3'	308
β2a	XM_011238946.2	Fwd: 5´-CACGGTGCCGCTTGGT-3´ Rev: 5´-TGCATGAAGAGGTGGCAGAA-3´ Probe: 5´-AAGCCACGCTCTGAC-3´	5´-UTR-ex2B	Fwd: 5´-ATATGTCGACTGGACAGTGGCCGTGACGAG-3 Rev: 5´-CTTGAAGCTTCACAGCCTTCTTTAACCAGC-3´	440
β2b	NM_001252533.1	Fwd: 5´-TTACACATCTCAAACTTCAGGGAAAA-3´ Rev: 5´-CCAGCTAAAGGTGGCTTTGC-3´	5´-UTR	Fwd: 5´-ATATGTCGACCGTTAGAAAGTCATGAAGTC-3´ Rev: 5´-CTTGAAGCTTCACAGCCTTCTTTAACCAGC-3´	523

		Probe: 5´-CGGAGCCCGTGCGA-3´			
β2c+d	XM_006497314.3 NM_023116.4	Fwd: 5´-AAAGGCTCGGATGGAAGCA-3´ Rev: 5´-CCCTGGCGGACAAAACTGT-3´ Probe: 5´-ATCGTCAGACACTACCTC-3´	ex2A-3	Fwd: 5´-ATATGTCGACTTGCCGATGGTCCAAAGCGAC-3´ Rev: 5´-CTTGAAGCTTCACAGCCTTCTTTAACCAGC-3´	519
β2e	NM_001309519.1	Fwd: 5´-GGGAGGAAGGCTGAAGAGTTC-3´ Rev: 5´-GGGCGGCTGGTGTAGGA-3´ Probe: 5´-ACATCTGTGGTTCGGC-3´	ex2D-3	Fwd: 5´-ATATGTCGACCTACCCGGCTCATGAAGGCCACCTGG-3´ Rev: 5´-CTTGAAGCTTCACAGCCTTCTTTAACCAGC-3´	392

Supplemental Table 1. TaqMan assays for β1-4 isoforms and N-terminal β2 splice variants including cDNA specific primer sequences for standard template cloning. Additional SalI and HindIII restriction enzyme sites (see Methods) are underlined; the reverse (rev) primer used for standard template cloning including the HindIII restriction site was the same for β2a-e subunit variants; rev, reverse; fwd, forward.

gene symbol	name	cellular function	assay ID
Actb	beta-actin	cytoskeletal protein	Mm00607939_s1
B2m	beta-2-microglobulin	immunity protein	Mm00437762_m1
Gapdh	glyceraldehyde-3-phosphate dehydrogenase	oxidoreductase	Mm99999915_g1
Hprt1	hypoxanthine phosphoribosyl-transferase 1	transferase	Mm00446968_m1
Tbp	tata box binding protein	transcription factor	Mm00446973_m1
Tfrc	transferrin receptor	receptor	Mm00441941_m1
Sdha	succinate dehydrogenase complex, subunit A	oxidoreductase	Mm01352363_m1

1376

1377 **Supplemental Table 2. Names, cellular functions and assay ID's of endogenous control**
1378 **genes.**

1379 For details see methods.

1380

β-subunit	B	SE-B	Y-int.	SE-Y	R^2	LOD	LOQ	E (%)
β1	-3.246	0.009	35.15	0.13	0.997	5	100	103
β2	-3.382	0.024	37.81	0.24	0.996	5	30	98
β3	-3.263	0.032	35.30	0.16	0.995	5	50	103
β4	-3.231	0.032	36.48	0.38	0.994	10	100	104
β2a	-3.283	0.037	35.04	0.54	0.981	10	100	101
β2b	-3.334	0.070	34.36	0.14	0.990	10	120	99
β2c+d	-3.160	0.023	35.78	0.02	0.998	5	20	107
β2e	-3.070	0.005	35.30	0.12	0.993	5	50	111

Supplemental Table 3. Quantitative RT-PCR standard curve parameters.
SE-B,-Y, standard error of B and Y-intercept; Y-int., Y-intercept (CT value); R^2, squared correlation coefficient; LOD, limit of detection (number of transcripts); LOQ, limit of quantification (number of transcripts); E (%), Efficiency in % (E=10-1/slope-1), 100% efficiency corresponds to a slope of -3.32.

	A. mRNA expression in SN DA neurons of juvenile wildtype mice				
analyzed mRNA	**mean**	**±SD**	**±SEM**	**median**	**n/N**
β2	0.15	0.13	0.04	0.16	10/1

	B. number of mRNA molecules in DA neurons of adult wildtype mice									
	SN					**VTA**				
analyzed mRNA	**mean**	**SD**	**SEM**	**median**	**N**	**mean**	**SD**	**SEM**	**median**	**N**
β2a	4.72	0.40	0.16	4.86	6	4.62	0.42	0.17	4.67	6
β2e	9.68***	1.76	0.72	10.25	6	8.43***	1.93	0.79	8.13	6

Supplemental Table 4: Single cell gene expression data.

Data and statistics of genes as indicated for graphs shown in Suppl Fig. 2C (middle) and D (right). n represents number of analyzed dopaminergic neurons derived from N individual mice. Significances according to two-way ANOVA followed by Tukey's multiple comparisons test: ***, $p<0.001$.

Gene	Primer	Sequence (5`-3`)	Genbank accession no. (NCBI)	5`-Position	Amplicon size [bp]
Mouse Calbindin-d28k (CB)	F (outer)	CGCACTCTCAAACTAGCCG	M21531	87	891
	R (outer)	CAGCCTACTTCTTTATAGCGCA		977	
	F (inner)	GAGATCTGGCTTCATTTCGAC		167	440
	R (inner)	AGTTCCAGCTTTCCGTCATTA		606	
Mouse Glial fibrillary acidic protein (GFAP)	F (outer)	AGAACAACCTGGCTGCGTAT	K01347	407	786
	R (outer)	GCTCCTGCTTCGAGTCCTTA		1192	
	F (inner)	AGAAAGGTTGAATCGCTGGA		472	517
	R (inner)	CCAGGGCTAGCTTAACGTTG		988	
Mouse Glutamate decarboxylase (GAD65)	F (outer)	CATACGCAGACAGCACGTTT	NM_008078.1	166	905
	R (outer)	AAAAGATTCCATCGCCAGAG		1070	
	F (inner)	GGGATGTCAACTACGCGTTT		606	389
	R (inner)	CACAAATACAGGGGCGATCT		994	
Mouse Glutamate decarboxylase (GAD67)	F (outer)	TGACATCGACTGCCAATACC	Z49976	731	1105
	R (outer)	GGGTTAGAGATGACCATCCG		1835	
	F (inner)	CATATGAAATTGCACCCGTG		761	702
	R (inner)	CGGTGTCATAGGAGACGTCA		1462	
Mouse Tyrosine hydroxylase (TH)	F (outer)	CACCTGGAGTACTTTGTGCG	M69200	387	1139
	R (outer)	CCTGTGGGTGGTACCCTATG		1525	
	F (inner)	TGCACACAGTACATCCGTCA		936	377
	R (inner)	TCTGACACGAAGTACACCGG		1312	
Mouse Cav2.3 R-type calcium channel (Cacna1e)	F (outer II-III loop)	CCATCTACTTCATTGTGCTCACC	NM_009782.3	2043	816*
	R (outer II-III loop)	CCCCTTCATCCAGACTCCG		2858	
	F (outer C-terminus)	GACAGCAGCTGGAAGAACAGA		5670	641*
	R (outer C-terminus)	GATGGAGCTCTCACTTAGGGAAC		6310	
	F (inner II-II loop)	GGAGGTCAGCCCGATGTC		2203	420*
	R (inner II-III loop)	GGGCTCCTCTGGTTGTCC		2622	
	F (inner C-terminus)	CTGAGTGGTCGGAGTGGATAC		5795	369*
	F (innerC-terminus)	AGAGAGGAGGTGCTTTCGTTC		6163	

Supplemental Table 5: Multiplex PCR (outer) and nested PCR (inner) primers for qualitative PCR

F: forward primer, R: reverse primer

	Cav1.3$_L$ - Activation 15 mM Ca^{2+}						Cav1.3$_L$ - Inactivation 15 mM Ca^{2+}			
β-subunit	**$V_{0.5}$ [mV]**	**k [mV]**	**V_{rev} [mV]**	**act thresh [mV]**	**current density [pA/pF]**	**n**	**$V_{0.5, inact}$ [mV]**	**k_{inact} [mV]**	**plateau [%]**	**n**
β2a	4.3 ±1.8	10.0 ±0.3	71.2 ±2.0	-34.5 ±0.9	-7.8 ±0.6	14	-18.3 ±3.2	10.0 ±1.0	36.2 ±5.8	5
$^{C3S/C4S}$β2a	0.2 ±1.2	9.2* ±0.2	71.3 ±1.1	-34.9§§ ±0.9	-8.4 ±1.6	15	-24.4 ±1.1	6.1*** ±0.4	21.6* ±2.1	11
β3	3.1 ±1.9	8.9* ±0.4	71.1 ±2.7	-30.6* ±0.8	-10.2 ±1.4	9	-20.3 ±0.9	7.0* ±0.5	28.5 ±5.4	5

Cav1.3$_L$ - 5 s Inactivation 15 mM Ca^{2+}							
β-subunit	**r50 [%]**	**r100 [%]**	**r250 [%]**	**r500 [%]**	**r1000 [%]**	**r5000 [%]**	**n**
β2a	86.8 ±2.7	81.2 ±3.0	71.5 ±3.5	63.3 ±4.1	54.6 ±4.2	36.0 ±3.7	10
$^{C3S/C4S}$β2a	74.5* ±3.0	62.7*** ±2.6	47.1*** ±3.2	33.0*** ±2.6	23.3*** ±2.6	12.6*** ±1.7	14
β3	81.5 ±3.4	70.3 ±3.7	50.6** ±4.1	34.6*** ±3.9	25.2*** ±4.2	13.7*** ±3.0	7

Supplemental Table 6. Voltage-dependence of activation and inactivation of Cav1.3 co-transfected with α2δ1 and different β-subunits in tsA-201 cells

All values are given as mean ± SEM for the indicated number of experiments (N=2). Parameters were obtained as described in Materials and Methods from a holding potential of -89 mV using 15 mM Ca^{2+} as the charge carrier.

Voltage-dependence of gating: Parameters are as given in legend to Table 1. Statistical significance was determined using one-way ANOVA with Bonferroni post-hoc test ($V_{0.5}$, V_{rev}, act thresh, $V_{0.5,inact}$, k_{inact}, plateau) or Kruskal-Wallis followed by Dunn's multiple comparison test (k). Statistical significances of post hoc tests are indicated for comparison vs. β2a (*, **, ***) or vs. β3 (§, §§, §§§): *** $p<0.001$; ** $p<0.01$; * $p<0.05$.

Inactivation time course: The r values represent the fraction of I_{Ca} remaining after 50, 100, 250, 500, 1000 or 5000 ms during a 5-s pulse to V_{max}. Statistical significance was determined using one-way ANOVA with Bonferroni post-hoc test. Statistical significances of post hoc tests are indicated for comparison vs. β2a: *** $p<0.001$; ** $p<0.01$; * $p<0.05$).

Effect of SNX-482 (100 nM) on I_{Ca} peak amplitude (pA)					
	mean	SD	SEM	median	n/N
control	1220	372	131	1170	8/7
SNX-482	1070	342	121	1110	8/7
p-value	0.0276 (two-tailed paired t-test)				
Remaining I_{Ca} peak amplitude in SNX-482 (%)					
control vs. SNX-482	87	11	4	90	8/7
p-value	0.0122 (two-tailed one sample t-test)				
Effect of nifedipine (10 µM) on I_{Ca} peak amplitude (pA)					
	mean	±SD	±SEM	median	n
control	1240	351	143	1240	6/6
Nifedipine	1120	312	127	1120	6/6
p-value	0.0312 (two-tailed Wilcoxon test)				
Remaining I_{Ca} peak amplitude in nifedipine (%)					
control vs. Nifedipine	90	3	1.4	91	6/6
p-value	0.0312 (two-tailed Wilcoxon signed rank test)				

1417

1418 **Supplemental Table 7: Inhibition of I_{Ca} in SN DA neurons of adult (12 weeks) mice by**
1419 **100 nM SNX-482 and 10 µM nifedipine**

1420 For details see results.

1421 **Supplemental Methods**

1422 **Dissection of brain tissue for RT-qPCR**

1423 Tissue was dissected after mice had been sacrificed by cervical dislocation under isoflurane
1424 (Vetflurane, Vibac UK, 1000 mg/g) anesthesia. The freshly extracted mouse brains from 12-
1425 14 weeks old male mice were snap-frozen in isopentane (Carl Roth, catalog #3926.2) that was
1426 pre-cooled with dry ice (~-40°C). To dissect VTA and SN tissue, 100 µm thick sections were
1427 cut on a cryostat (CM1950, Leica, Germany) and collected on glass coverslips. After cooling
1428 the coverslips on dry ice, regions of interest were punched under a dissection microscope
1429 using a pre-cooled sample corer (Fine Science Tools, Germany) (VTA: inner diameter 0.8 mm,
1430 1 punch per hemisphere; SN: inner diameter 0.5 mm, 2 punches per hemisphere). For each
1431 brain region, tissue punches from both hemispheres of 7-8 successive 100 µm sections
1432 between Bregma -3.00 mm and -3.80 mm (according to Paxinos & Franklin, 2004) were
1433 collected in the sample corer. The tissue punches were transferred into an Eppendorf tube and
1434 again snap-frozen in liquid nitrogen. The punched brain sections were stained with cresyl violet
1435 (Nissl's staining) for histological verification. Briefly, the slides with the punched sections were
1436 incubated in 4% PFA overnight. On the next day, the sections were rinsed in H_2O and the
1437 following staining steps were performed: H_2O 1 min, 70% ethanol 5 min, 100% EtOH 5 min,
1438 0.5% cresyl violet solution pH 3.9 (2.5 g cresyl violet acetate, 30 ml 1M Na-acetate*3 H_2O and
1439 170 ml 1M acetic acid) 10 min, 70% ethanol 2 min, 100% ethanol 2 min, Xylol 1 min. The
1440 sections were coverslipped immediately with Eukitt (Sigma-Aldrich, catalog #03989), left to
1441 harden overnight and imaged on a bright field microscope at 2x.

1442 **RNA isolation and cDNA synthesis for tissue RT-qPCR**

1443 RNeasy® Lipid Tissue Mini Kit (Qiagen GmbH, Germany, catalog #1023539) was used to
1444 isolate total RNA from brain tissues. Briefly, the tissue was disrupted and homogenized by
1445 vortexing samples for 5-10 minutes in 500 µl (SN, VTA) of phenol/guanidine-based Qiazol lysis
1446 reagent (Qiagen GmbH, Germany, catalog #79306) and passing the lysate ten times through
1447 a 21-gauge needle. All further steps, including purification of RNA with QIAGEN silica gel
1448 membrane technology (Qiagen GmbH, Germany), were performed according to the
1449 manufacturer's protocol. For the final elution 15 µl of RNase-free water were used twice. An
1450 optional on-column DNase digestion (Qiagen GmbH, Germany, catalog #79254) was
1451 performed to reduce genomic DNA contamination. The RNA concentration was determined
1452 photometrically yielding approximately 20 ng/µl for VTA and SN or 1-2 µg/µl for whole brain.

1453 RNA was reverse transcribed using Maxima H Minus First Strand cDNA synthesis kit with
1454 random hexamer primers following the manufacturer´s instructions (Thermo Fisher Scientific,

1455 Waltham, MA, USA). 1 µg or 13 µl of total RNA were used as template for reverse transcription.
1456 1 µl cDNA corresponds to 0.65 x the amount of RNA equivalent.

1457

1458 **Standard curve method-based RT-qPCR for quantification of β-subunit expression in**
1459 **SN and VTA**

1460 In order to generate DNA templates of known concentrations for RT-qPCR standard curves,
1461 the concentration of the digested fragments was determined using the Quant-IT PicoGreen
1462 dsDNA Assay Kit (Invitrogen, Carlsbad, CA, USA). Subsequently, standard curves were
1463 generated using a serial dilution ranging from 10^7 to 10^1 DNA molecules in water containing 1
1464 *µ*g/ml of poly-dC DNA (Midland Certified Reagent Company Inc., Midland, TX, USA). RT-
1465 qPCRs of standard curves and samples were performed as described previously (N. J. Ortner
1466 et al., 2020; Schlick et al., 2010). Samples for RT-qPCR quantification (50 cycles) contained 5
1467 ng of total RNA equivalent of cDNA, the respective TaqMan gene expression assay, and
1468 TaqMan Universal PCR Master Mix (Thermo Fisher Scientific). Specificity of all assays was
1469 confirmed using different DNA ratios of corresponding and mismatched DNA fragments for the
1470 β1-4 and for the β2a-2e assays, respectively. Importantly, all assays specifically recognized
1471 the corresponding fragment even in the presence of a 10-fold higher concentration of other
1472 splice variants (Suppl. Fig. 1). RT-qPCR was performed in duplicates from three independent
1473 RNA preparations from three biological replicates. Samples without template served as
1474 negative controls. No RT RNA controls could not be included since all obtained RNA was
1475 transcribed into cDNA due to low yields. The expression of seven different endogenous control
1476 genes (*Actb*, *B2m*, *Gapdh*, *Hprt1*, *Tbp*, *Tfrc* and *Sdha*; N. J. Ortner et al., 2020; Schlick et al.,
1477 2010) was routinely measured and used for data normalization as previously described
1478 (Genome BiolVandesompele et al., 2002) (Suppl. Fig. 1, Suppl. Table 2). Briefly, data were
1479 normalized to the most stably expressed endogenous control genes (*Gapdh* and *Tfrc*)
1480 determined by geNorm (Suppl. Fig. 1). Normalized molecule numbers were calculated for each
1481 assay based on their respective standard curve. Standard curve parameters are given in
1482 (Suppl. Table 3). qPCR analyses were performed using the 7500 Fast System (Applied
1483 Biosystems, Foster Systems, CA, USA).

1484

1485 **Target probes for RNAScope *in situ* hybridization in identified SN DA and VTA DA**
1486 **neurons and image acquisition**

1487 Target probes were either obtained from the library of validated probes provided by Advanced
1488 Cell Diagnostics (ACD) or self-designed in cooperation with ACD to specifically discriminate

between two splice variants of β2, namely β2a and β2e. Target probes (RNAScope assays) used for analysis were as follows:

Gene	Cat No. (ACD)	Assay target region according to respective Genbank accession no. (NCBI)
Tyrosine hydroxylase	317621	483 – 1603 of NM_009377.1
β2a (*Cacnb2a*)	590951-C2	2-296 of XM_011238946.2
β2e (*Cacnb2e)*	823221-C2	2-285 of NM_001309519.1

Target genes, visualized with Atto550 fluorophore, were co-stained with Tyrosine hydroxylase (TH), visualized with AlexaFluor488, as a marker for dopaminergic neurons. The gene peptidyl-prolyl isomerase B (PPIB) was used as positive control.

Fluorescent images of midbrain sections were acquired by a Leica CTR6 LED microscope using a Leica DFC365FX camera as z-stacks, covering the full depth of cells at 63x magnification. Z-stacks were reduced to maximum intensity Z-projections using Fiji (http://imagej.net/Fiji) and images were analyzed by utilizing a custom-designed algorithm (Wolution, Munich, Germany). The algorithm delineates cell shapes according to the TH marker gene signal and quantifies the area of fluorescent staining. According to Advanced Cell Diagnostics (ACD), target probe hybridization results in a small fluorescent dot for each mRNA molecule, allowing quantification of absolute number of mRNA molecules independent from fluorescent signal intensity.

Multiplex-nested PCR, qualitative and quantitative PCR analysis in identified DA neurons

Cryosectioning, laser-microdissection, reverse transcription: Cryosectioning, UV-laser microdissection (UV-LMD) and reverse transcription were carried out similarly as previously described in detail (Benkert et al., 2019; Duda et al., 2018; Grundemann et al., 2011; Liss, 2002). Briefly, coronal 12 µm mouse midbrain cryosections were cut with a cryomicrotome CM3050 S (Leica), mounted on PEN-membrane slides (Mirodissect), stained with a cresyl-violet (CV) ethanol solution and fixed with an ascending ethanol series. UV-LMD of SN dopaminergic neurons from cresyl-violet-stained midbrain sections from juvenile mice was carried out using an LMD7000 system (Leica Microsystems). Reverse transcription was carried out directly without a separate RNA isolation step in a one-tube procedure.

All cDNA samples were precipitated as described (Liss, 2002). Qualitative multiplex-nested PCR and quantitative qPCRs were carried out essentially as described (Benkert et al., 2019; Duda et al., 2018; Grundemann et al., 2011). Briefly, qualitative multiplex-nested PCR was

1522 performed with the GeneAmp PCR System 9700 (Thermo Fisher Scientific) using 1/3 of each
1523 individual cDNA sample, corresponding to ~3 SN DA neurons, for marker gene expression
1524 analysis: tyrosine hydroxylase (TH) as a marker for dopaminergic midbrain neurons, the
1525 glutamic acid decarboxylase isoforms GAD_{65} and GAD_{67} as markers for GABAergic neurons,
1526 the glial fibrillary acidic protein (GFAP) as a marker for astroglia cells and calbindin d28k
1527 (CBd28k), that is strongly expressed only in less vulnerable dopaminergic midbrain neurons.
1528 Only cDNA pools expressing the correct marker gene profile (i.e., TH positive, GAD, GFAP,
1529 CBd28k negative) were further analyzed via qualitative and quantitative PCR. Qualitative PCR
1530 for β2 splice variant expression analysis was performed with the QuantStudio 3 System
1531 (Thermo Fisher Scientific) using ~3 SN DA neurons. Qualitative PCR products were analyzed
1532 in a QIAxcel Advanced System (Qiagen).

1533 Details of multiplex PCR (outer) and nested PCR (inner) primers for qualitative PCR are
1534 shown in Suppl. Table 5.

1535 For Cav2.3 splice variant analysis via qualitative RT-PCR, two cDNA fragments (mCav2.3 II-
1536 III loop and mCav2.3 C-terminus) covering the three respective splice sites were amplified in
1537 a duplex PCR, followed by two individual nested PCR reactions. PCR conditions: 15 min 95°C;
1538 35 cycles: 30 s 94°C; 1 min 61°C; 3 min 72°C; 7 min 72°C for duplex PCR; and 3 min 94°C;
1539 35 cycles: 30 s 94°C; 1 min 61°C; 1 min 72°C; 7 min 72°C for nested PCRs. Primer sequences
1540 are given in Supplementary Table 2. Outer duplex primer pairs were chosen using Oligo7.60
1541 software (possible PCR amplicon sizes for mCav2.3 II-III loop: 816 bp, 795 bp and 759 bp; for
1542 mCav2.3 C-terminus: 770 bp and 641 bp). For the nested PCRs, primer sequences from
1543 Weiergraber et al., 2005 were used (possible PCR amplicon sizes for mCav2.3 II-III 980 loop:
1544 420 bp, 399 bp and 363 bp; for mCav2.3 C-terminus: 498 bp and 369 bp). Nested PCR
1545 products were separated in a 4% agarose gel (MetaPhor agarose, Biozym), and expressed
1546 splice variants in individual SN DA neurons were identified according to the amplicon sizes of
1547 the nested PCR products (cDNA from mouse whole-brain tissue was used as positive control)
1548 as follows (II-III-loop + C-terminus): Cav2.3a: 363 + 369 bp; Cav2.3b: 399+369 bp; Cav2.3c:
1549 420+369 bp; Cav2.3d. 420+498; Cav2.3e: 363 + 498 bp; Cav2.3f: 399 + 498 bp.

1550 Quantitative real time PCR (qPCR) was performed with the QuantStudio 3 System (Thermo
1551 Fisher Scientific). qPCR assays (TaqMan®), were marked with a 3' BHQ (black hole quencher)
1552 and 5' FAM (Carboxyfluorescein). TaqMan assays were carefully established and performance
1553 was evaluated by generating standard curves, using defined amounts of cDNA (derived from
1554 midbrain tissue mRNA), over four magnitudes of 10-fold dilutions as templates, in at least three
1555 independent experiments, as described (Duda et al., 2018; Liss, 2002).

1556 Details of all qPCR assays (TaqMan®), and standard curve parameters used for analysis are
1557 provided in Supplementary Table 4.

1558 Relative qPCR quantification data are given as cDNA amount [pg/cell] with respect to midbrain-
1559 tissue cDNA standard curves, calculated according to the following formula, and were
1560 normalized to the respective cell size by dividing respective expression values to the
1561 corresponding area of the individual microdissected neurons.

1562 $$DNA\ amount\ per\ cell\ [\frac{pg}{cell}] = \frac{S^{[(Ct - Y_{intercept})/slope]}}{No_{cells} \cdot cDNA\ fraction}$$

1563 With S = serial dilution factor of the standard curve (i.e. 10), No_{cells} = number of SN DA neurons
1564 per sample (i.e. 10 here), cDNA fraction = fraction of the cDNA reaction used as template in
1565 the qPCR reaction (i.e. 5/17) and the Y-intercept and slope of the relative standards (see
1566 Supplementary Table 4).

1567 β2 TaqMan qPCR assay and standard curve information, used for relative qPCR-based
1568 transcript quantification: Note that the amplicon is very small (70 bp). The probe is 5'-FAM (6-
1569 carboxyfluorescein) and 3'-NFQ (non-fluorescent quencher) labelled. The assay
1570 Mm01333550_m1 (assay-ID) was used (assay location 583) spanning exon-boundary 4-5 of
1571 the mouse β2 gene (*Cacnb2*). Assay parameters were as follows: threshold for analysis: 0.05,
1572 Y-intercept of standard curve: 43.5 ± 0.2, slope: -3.43 ± 0.04, R^2: 1.0 ± 0.0: means ± SEM,
1573 n=5.

1574

1575 **Slice preparation for perforated patch recordings in SN DA neurons**

1576 Animals were anesthetized with isoflurane (B506; AbbVie Deutschland GmbH and Co KG,
1577 Ludwigshafen, Germany) and subsequently decapitated. The brain was rapidly removed and
1578 a block of tissue containing the mesencephalon was immediately dissected. Coronal slices
1579 (250 - 300 µm) containing the SN were cut with a vibration microtome (HM-650 V; Thermo
1580 Scientific, Walldorf, Germany) under cold (4°C), carbogenated (95% O_2 and 5% CO_2), glycerol-
1581 based modified artificial cerebrospinal fluid (GACSF; Ye et al., 2006) containing (in mM): 250
1582 glycerol, 2.5 KCl, 2 $MgCl_2$, 2 $CaCl_2$, 1.2 NaH_2PO_4, 10 HEPES, 21 $NaHCO_3$, 5 glucose adjusted
1583 to pH 7.2 (with NaOH) resulting in an osmolarity of ~310 mOsm. Brain slices were transferred
1584 into carbogenated artificial cerebrospinal fluid (ACSF). First, they were kept for 20 min in a
1585 35°C 'recovery bath' and then stored at room temperature (24°C) for at least 30 min prior to
1586 recording. ACSF contained (in mM): 125 NaCl, 2.5 KCl, 2 $MgCl_2$, 2 $CaCl_2$, 1.2 NaH_2PO_4, 21
1587 $NaHCO_3$, 10 HEPES, and 5 Glucose adjusted to pH 7.2 (with NaOH) resulting in an osmolarity
1588 of ~310 mOsm.

1589 SN dopaminergic neurons were identified according to their sag component / slow Ih-current,
1590 broad action potentials or post hoc by TH/DAT-immunohistochemistry (Lacey et al., 1989;

Neuhoff et al., 2002; Richards et al., 1997). Biocytin-streptavidin labeling was combined with TH-immuno-histochemistry (Hess et al., 2013).